NASA TT F-10,716

INVESTIGATION OF COMPRESSED GAS DISPERSION IN RELATION TO ITS APPLICABILITY IN GAS TURBINE ENGINES

H. Gehrig

Translation of "Untersuchung der Druckgaszerstäubung im Hinblick auf ihre Anwendbarkeit in Gasturbinen-Triebwerken." Darmstadt Technische Hochschule, Darmstadt, 102 pp, 1965.

N68-10176
(ACCESSION NUMBER) (THRU)
91 1
(PAGES) (CODE)
(NASA CR OR TMX OR AD NUMBER) (CATEGORY)
FF No. 602(C)
AVAILABLE TO U.S. GOVERNMENT AGENCIES ONLY

NATIONAL AERONAUTICS AND SPACE ADMINISTRATION
Washington, D.C. 20546 March 1967

Reproduced by the CLEARINGHOUSE for Federal Scientific & Technical Information Springfield Va. 22151

ANNOTATION

A dissertation approved by the Faculty for Machine-building in Darmstadt Technical College in fulfillment of the requirements for the degree of Doctor of Engineering.

This project is part of a research study of the DFG [German Research Association] aeronautical research program under the direction of the research leader H. Triebnigg, Professor, Doctor of Engineering. His basic ideas and findings form the basis of the investigations performed.

I want to express my sincere thanks to my revered teacher for his many suggestions, valuable advice, and generous support; I dedicate this project to him.

I am also indebted to my team mate, H. Kühl, Professor, Doctor of Engineering Aachen Technical College and the German Aviation Testing Institute in Porz-Wahn) for his constructive criticism and suggestions for improvement.

Darmstadt, 1965

TABLE OF CONTENTS

		Page
	PART I	
1.	Introduction	2
2.	Outline and Purpose of Project	3
3.	Derivation and Extension of Atomization Law	4
4.	Characteristics of a Jet Stream	7
5.	Design of Spray Diffusers	9
6.	Energy Considerations	13
6.1.	Theoretical Pressure Recovery	13
6.2.	Actual Pressure Recovery	15
6.3.	Permissible Energy Expenditure in Case of Air Injection	15
7.	Experimental Investigation of the Relations Between Jet Parameters and Penetration Depths	16
7.1.	Jet Parameters (Nozzle Parameters)	16
7.1.1.	Flow rate parameters	16
7.1.2.	Nozzle impulse parameters	19
7.1.3.	Nozzle efficiency	23
7.1.4.	Jet angle	26
7.2.	Penetration Depths (Jet Contours)	28
7.2.1.	Test Section, measurement method, and measurement accuracy	28
7.2.2.	Jet contours in the case of parallel stream injection	29
7.2.3.	Cross-stream injection	34
7.2.4.	Reverse-flow injection	37
8.	Flameholder and Nozzle Jet (Low Temperature Experiments)	39
8.1.	Summarizing Evaluation of the Various Principal Combustion Chamber Flameholders	39
8.2.	Afterburning Chamber Flameholder in the Nozzle Jet	41
8.2.1.	Parallel air injection	41
8.2.2.	Injection of cross-stream	43
8.2.3.	Reverse-flow insufflation	44
9.	Distribution Measurements	46
9.1.	Without Flameholder	46
9.2.	With Flameholder	48
10.	Investigations of Contour with Changed Restrictions	49
10.1.	Atomization of Fuel in Cold Air	49
10.2.	Atomization of Water in Hot Gas	49
11.	Observation of the Relative Droplet Sizes	52
11.1.	Atomizing Air Ratio and Relative Droplet Size	52
11.2.	Hot Air Atomization and Relative Droplet Size	53
11.3.	Ambient Pressure and Relative Droplet Size	56
	PART II	
12.	General Test Installation and Data Concerning Experimental Combustion Chamber	59

12.1.	General Test Installation	59
12.2.	Test Chamber	61
13.	Temperature Determination	65
14.	Combustion Determination	66
14.1.	Combustion Determination from the Rise in Temperature	66
14.2.	Combustion Determination from Gas Analyses	68
15.	Experimental Investigation of the Influence of Combustion and Ignition Limits	71
15.1.	Investigation of the Parameters Influencing Combustion	71
15.2.	Investigation of Parameters Influencing Ignition Limits	73
16.	First Afterburning Tests	74
16.1.	Outline and Conduct of the Experiments	74
16.2.	Parallel Jet Injection	76
16.2.1.	Injection in front of a simple angular flameholder	76
16.2.2.	Parallel jet injection in front of combined flameholder	79
16.3.	Diagonal Reverse-flow Injection Behind Flameholders	81
16.4.	Direct Reverse-flow Injection	83
17.	Summary	85
	References	87

Compilation of Essential Notations

p	mmWC; kg/cm^2	pressure
t	°C	temperature
T	°K	absolute temperature
γ	kg/m^3	specific weight
ρ	$kg \cdot sec^2/m^4$	density
R	kg-m/kg·deg	gas constant
g	m/sec^2	terrestrial acceleration
κ	-	adiabatic exponent
i	kcal/kg	enthalpy
H	m	head, pressure head
π	-	pressure ratio
c	m/sec	velocity
M	-	Mach number
σ	kg/m; dyn/cm	surface tension, capillary constant
ν	m^2/sec	kinematic viscosity
η	$kg \cdot sec/m^2$	dynamic viscosity
Re	-	Reynolds number
We	-	Weber number
Ge	-	Reynolds number/Weber number
C_R	-	resistance coefficient
C_P	kcal/kg·deg	specific heat
d	mm,m	diameter
F	mm^2, m^2	area, cross section
μ	-	chamber air ratio
λ_{AN}	-	atomizing air ratio
λ, λ_{tot}	-	excess air number
λ_{pr}	-	primary excess air number
b_l	-	specific fuel consumption
ℓ_l	-	specific air consumption
α_{jet}	o	half jet angle
α_M	o	mushroom angle
α_{Tq}	o	torque angle
α_O	o	orbital angle
β	o	injection angle
Δ	-	difference
$x; y$	mm	jet coordinates, penetration depth
$\xi; \eta$		transformed jet coordinates
η_N	%	nozzle efficiency
η_M	%	mixture efficiency

S	kg	thrust
I	kg	momentum
R	kg	resistance
A	kcal/kg-m	mechanical heat equivalent
E	kg-m/hr	temporal energy, performance
s	mm	travel
s	-	blocking air exponent
r	-	blocking liquid exponent
k_B	-	blocking factor of the nozzle
k_{Bmax}	-	maximum linear blocking factor
K_N	-	air momentum-nozzle constant
i	-	air momentum exponent for all nozzles
K_F	-	nozzle constant of fictive jet velocity
n	-	air exponent of fictive jet velocity
m	-	liquid exponent of fictive jet velocity
K_α	-	jet angle constant
t_L	sec	lifetime
t_I	sec	ignition delay
t	min	measuring time, collection time
h	min	catch height
h	-	parts by weight of hydrogen per kg fuel
c	-	parts by weight of carbon per kg fuel
O_{min}	Nm^3/kg	minimum oxygen volume per kg fuel
V_{Gdr}	Nm^3/kg	volume of dry gas per kg fuel
v_{CO}	Nm^3/Nm^3	relative CO volume
$H_{\ell CO}$	kcal/Nm^3	lower heating value of CO
H_ℓ; $H_{\ell F}$	kcal/kg	lower heating value of fuel
Q_{su}	kcal/hr	heat supply into chamber
Q_{CO}	kcal/hr	heat still present in total CO
q_{CO}	kcal/kg	heat still present in CO per kg fuel
η_{CCO}	%	combustion, considering solely the unburnt CO
$\overline{\eta}_C$	%	combustion from heat balance
η_C	%	combustion from actual and theoretical temperature increase
η_{Ctot}	%	total combustion from main combustion chamber and afterburning
b	mm	width of flameholder

ϕ	%	blockage of flameholder
T_R	°K	rated temperature
L	kcal/hr·m^3·atm abs	thermal load of combustion chamber
V	m^3	volume
V_{Flt}	m^3	flame tube volume
V_{CoC}	m^3	combustion chamber volume
V_{MC}	m^3	mixing chamber volume
ℓ_{CoC}	m	combustion chamber length
ℓ_C	m	combustion length, flame length
$\ell_{\ell S}$	m	separation length
K_{CL}	-	combustion length characteristic
K_p	-	profile factor

Subscripts:

0, 1, 2, 3, 4, 5, 6 — measuring locations

A	air
G	gas
F	fuel
W	water
Fl	fluid
CC	combustion chamber
AB	afterburning
AN	atomizing nozzle
N	nozzle
FlH	flameholder
Dr	droplet
Bn	boundary
tot; t	total
st	static
dyn	dynamic
a	atmospheric
ad	adiabatic
cr	critical
th	theoretical
act	actual
f	fictive
perm	permissible
max	maximum
min	minimum
ax	axial
rad	radial
tan	tangential
m	meridian
m	mean
pr	primary
sec	secondary
c	cold
h	hot
dr	dry
∞	at a very large distance

N68-10176

INVESTIGATION OF COMPRESSE GAS DISPERSION IN RELATION TO ITS APPLICABILITY IN GAS TURBINE ENGINES

H. Gehrig

National Aeronautics and Space Administration
Washington, D.C.

March 1967

CLEARINGHOUSE
FOR FEDERAL SCIENTIFIC AND TECHNICAL INFORMATION

U. S. DEPARTMENT OF COMMERCE / NATIONAL BUREAU OF STANDARDS / INSTITUTE FOR APPLIED TECHNOLOGY

INVESTIGATION OF COMPRESSED GAS DISPERSION IN RELATION TO ITS APPLICABILITY IN GAS TURBINE ENGINES

Heinz Gehrig

A Contribution to Practical Applications

ABSTRACT. This is a study of the effect of the various nozzle types in terms of geometric configuration on certain jet characteristics in order to find a basically useful nozzle design for various types of practical application. On the basis of a systematic evaluation of a number of nozzle characteristics an attempt will be made to determine the extent to which general diagrams may be derived for all nozzle types so that it will become possible to arrive at a conclusion concerning jet impulse and its components. Parameters characterizing attainable penetration depths are established. A comparative evaluation of the contour diagrams and nozzle parameters serves to provide basic relationships significant for the design of the combustion chamber and selection of the nozzle type. Guidelines for flameholder configurations and nozzle arrangements, and for flameholders in the main and afterburning chambers are obtained by introducing various flameholders into or in front of the hot jets. The determinations are preferably conducted in the cold state at first and later in the high-temperature state in order to establish any deviations. In the high-temperature tests, the main combustion chamber is considered with special emphasis on the determination of preparation and combustion lengths. The effect of the mass ratio between atomization air and fuel on the ignition boundaries and on burnout are investigated and the most suitable operating conditions are established. Owing to the large number of problems involved, a certain selectivity had to be exercised in the project. An attempt is made to select some of the essential factors for study with the aim of obtaining a contribution to practical application and to lay a foundation for future investigations.

PART 1

1. Introduction

The processes that take place in a combustion chamber may be roughly separated into the following categories: /7

1) Atomization of fuel
2) Evaporation of drops and formation of mixture
3) Ignition
4) Fuel reactions with atmospheric oxygen
5) Heat-transfer processes in combustion chamber
6) Admixture of secondary air.

In order to channel the energy contained in the fuel into an operational process, it is necessary to distribute the energy carrier in the combustion chamber in as finely dispersed a form and as homogeneously as possible. This is primarily the job of the fuel nozzle. It causes dissociation by transforming a high fuel pressure (pressure injection) into kinetic jet energy or by utilizing the effects of compressed air or gas (pneumatic atomization.) The high exit velocity or relative velocity, in conjunction with the surrounding medium, causes the fragmentation of the jet into a large number of small droplets. As they are propagated, their velocity and size decrease. The dissociation of the jet into microdroplets results in a significant increase of the total surface of the liquid. In this way we get suitable prerequisites for evaporation and combustion of the fuel.

The currently most frequently employed method for fuel supply into the combustion chamber of gas turbine propulsion units is high-pressure injection (on the order of 100 atü). Here we get poor atomization in the small load ranges. In some instances so-called duplex nozzles are used to remedy the situation. Another method for attaining good atomization in the entire operational range, and also for making do without high-pressure pumps and high-pressure conduits, involves the atomization of the fuel by means of compressed air or pressure gas. Duplex nozzles are required for this purpose. The two media are fed into these nozzles under low pressure (order of magnitude of 1% of the values required in pressure injection.) The presence of the atomizing air in the jet stream offers yet another advantage because it enables us to anticipate an improvement in the initiation of the reaction processes and thus a faster conclusion of combustion. This advantage results in further savings in terms of construction. The turbine head may be used by employing the atomizing system in the afterburning chamber, i.e., air may be branched off either after the compressor or gas may be branched off after the combustion chamber to charge [load] the atomizing nozzles in the afterburner.

2. Outline and Purpose of Project

Part I contains first of all the formulation of an atomization law and a brief characterization of the essential factors affecting atomization. This work will not cover investigations on the dissociation process itself. The atomization nozzle will be shown to be the most important component in the characterization of the jet properties. The effect of the various nozzle types in terms of geometric configuration on certain jet characteristics will be investigated in the first main portion of this report. The aim will be to find basically useful nozzle designs for each type of practical application. An attempt will then be made to answer the question as to the permissible energy expenditure for pneumatic or compressed gas atomization. /8

On the basis of a systematic evaluation of a number of nozzle characteristics, an attempt will be made to determine the extent to which general diagrams may be derived for all nozzle types. It is hoped that this will make it possible to arrive at a conclusion regarding jet impulses and their components. These, together with the throughput data, will presumably characterize the most important parameters affecting the attainable penetration depths. In order to determine the penetration depths, the jet contours must be established for stationary and moving air atomization under various velocities and blow directions. A comparative evaluation of the contour diagram and of the nozzle parameters should result in the formulation of basic relationships which are of significance in designing the combustion chamber and in the selection of the nozzle type. Guidelines for flameholder configurations and nozzle arrangements, and for flameholders in the main and afterburning chambers, are obtained by introducing various flameholders into or in front of the jet streams. These experiments are preferably conducted first in the cold state, to be followed by experiments at high temperatures to establish any deviations.

In the high temperature tests reported in Part II, the main combustion chamber is given primary consideration. Suitable flameholder types are developed first; this is followed by the designing and constructing of a suitable test chamber. These operations are based on burnout parameters and distributions at the chamber exit. The effect of the mass ratio between atomization of air and fuel on the ignition boundaries and on burnout will be investigated, and the most suitable operating conditions will be established.

In the high temperature afterburning tests, special emphasis will be placed on the determination of the preparation and combustion lengths, and of the operating parameter ranges as functions of intake temperature and intake velocity, of flameholder configuration and flameholder size, of amount of fuel or air excess factor atomizing air ratio, and atomizing air temperature. Of course, this study is concentrated only on the first afterburning tests in which the goal is to establish the most suitable nozzle and flameholder arrangement over a half open measuring section. We furthermore hope to obtain data in these preliminary tests on the extent of the effects of the many parameters and their trends. /9

Because of the large number of problems involved in this atomization system, a certain degree of selectivity had to be exercised in this project. An attempt was made to select some of the essential factors for study so as to make a contribution to practical applications and to lay the foundation for subsequent investigations.

3. Derivation and Extension of the Atomization Law

The dissociation of jets of liquids in air has been investigated by researchers for several decades. Some of the results obtained will be briefly discussed here to establish the principal factors involved in atomization. A new formulation of the atomization law will be derived to extend the present one. The factors affecting atomization can be classed in three groups:

1) the physical properties of the liquid to be atomized,
2) the flow parameters in the jet, and
3) state and properties of the surrounding medium.

In practical injection systems of the hydraulic or pneumatic type, nozzle velocities of over 50 m/sec are employed in almost all instances. In most cases, spontaneous dissociation is observed immediately at the mouth of the nozzle. The dimensions of the droplets in the jet vary considerably (1:50 to 1:100); the distribution of the various sizes reveals certain frequencies. A plot of frequency against droplet diameter shows a bell-shaped (unsymmetrical) distribution curve. The average droplet size (maximum of the distribution curve) is also of interest in the evaluation of atomization quality, as is the maximum droplet size in the jet. Whereas it is possible to establish a theoretical ratio for the droplet size, it is not possible to characterize the distribution curves by computation alone.

The basic law, /10

$$d \sim \frac{\sigma}{p_{A\,dyn}} \sim \frac{\sigma}{\rho_A \cdot c_A^2} \qquad (1)$$

is known (Triebnigg, Scheubel, Weber, etc.). In this equation

d represents the theoretical droplet diameter,
σ represents the surface tension per unit length (capillary constant),
c_A represents the relative velocity between droplet and surrounding medium,
ρ_A represents the density of the surrounding medium.

It is also known that a small droplet assumes a spherical configuration owing to molecular forces, and that it develops a surface pressure of

$$p_o = \frac{4\sigma}{d} \qquad (2)$$

A droplet force balance is set up to establish the dissociation criterion. A droplet will remain stable until the resistance is smaller than

the surface force. The equilibrium state can be approximated in the Stokes range by the following expression:

$$p_o \cdot F = C_R \cdot p_{Adyn} \cdot F \tag{3}$$

Here F represents the projected droplet surface and C_R represents the resistance coefficient of the droplet. By inserting the value of p_o from Equation (2) into (3), the following solution is obtained with respect to d:

$$d = \frac{4\sigma}{C_R \cdot p_{Adyn}} = \frac{8\sigma}{C_R \cdot \rho_A \cdot v_A^2} \tag{4}$$

In atomization problems, the Weber number is often considered as the characterizing value; using this value, the atomization law looks like this:

$$d = \frac{\sigma}{\rho_A \cdot v_A^2} \cdot We \tag{5}$$

The following equation thus applies:

$$We = d \cdot \frac{\rho_A \cdot v_A^2}{\sigma} = \frac{8}{C_R} = 8 \frac{p_{Adyn}}{p_o} \tag{6}$$

Since the droplets may be considered spherical, the resistance values may be characterized with the corresponding values for spheres surrounded by flow. These are shown in Figure 1 (curve 1) plotted against the Reynolds number. The latter is defined as

$$Re = \frac{v_A \cdot d}{\nu_A} \tag{7}$$

where ν_A represents the viscosity of the surrounding medium. According to Stokes, Oseen, and Dallavalle, there exist approximating equations in certain regions for the function $C_R = f(Re)$ (see Figure 1, Curves 2, 3, and 4).

Along with curves 5 and 6, two of my own relations have been plotted here. These provide considerably better correlation with the actual C_R values:

I: For $Re < 400$ (< 700), $$C_R = \frac{12}{Re} \cdot \sqrt{4 + Re} \tag{8}$$

II: For (60<) $100 < Re < 10^4$ ($<10^5$), $$C_R = \frac{0.4}{Re} \cdot (200 + Re) \tag{9}$$

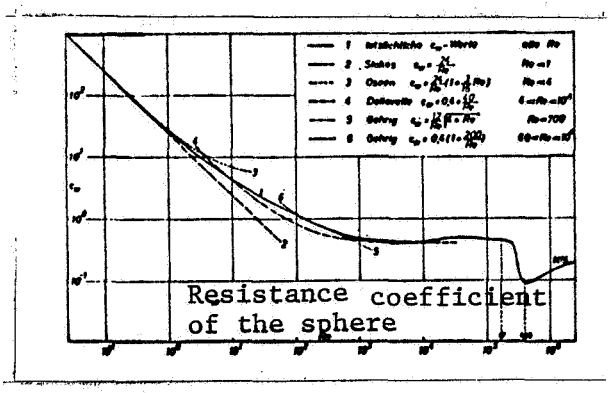

Figure 1

1 actual C_R values — all Re

2 Stokes $C_R = \frac{24}{Re}$ — $Re < 1$

3 Oseen $C_R = \frac{24}{Re}(1+\frac{3}{16}Re)$ — $Re < 4$

4 Dallavalle $C_R = 0.4 + \frac{40}{Re}$ — $4 < Re < 10^4$

5 Gehrig $C_R = \frac{12}{Re}\sqrt{4 + Re}$ — $Re < 700$

6 Gehrig $C_R = 0.4(1 + \frac{200}{Re})$ — $60 < Re < 10^4$

1 $f(Ge) = Re$

2 $Re = 20(Ge-10)$

3 $Re = (\frac{2}{3}Ge)^2-4$

4 $Re \to 0$ for $Ge \to 3$

5 $Ge = \frac{\delta}{c_A \eta_A} \quad \frac{Re}{We}$

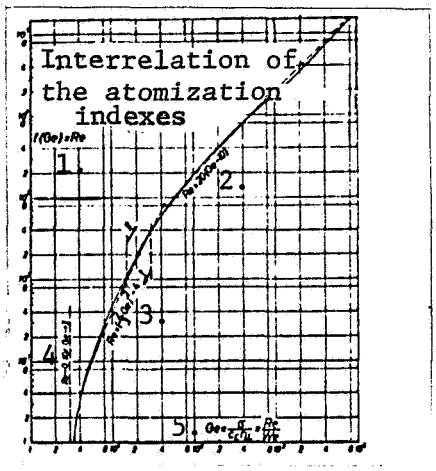

Figure 2

By combining equations (4) and (7), the following equation is obtained: /11

$$Re = \frac{c_A \cdot d}{\nu_A} = c_A \cdot \frac{\rho_A}{\eta_A} \cdot \frac{8\sigma}{c_R \cdot \rho_A \cdot c_A^2}$$

From this, the following equation follows:

$$c_R \cdot Re = 8 \cdot \frac{\sigma}{c_A \cdot \eta_A} \qquad (10)$$

The dimensionless value $\sigma/c_A\eta_A$ is defined as Ge. The following equation will apply:

$$Ge = \frac{\sigma}{c_A \cdot \eta_A} = \frac{Re}{We} \qquad (11)$$

The value Ge has an advantage over values Re and We in that it can be established without knowing the droplet diameters. The following results from equations (8), (9), and (10):

$$\text{I: For } 3 < Ge < 30,\ Re = \left(\frac{2}{3} Ge\right)^2 - 4 = f_1(Ge) \tag{12}$$

$$\text{II: For } 15 < Ge < 10^4,\ Re = 20.\ (Ge - 10) = f_{II}(Ge) \tag{13}$$

In Figure 2 we have plotted Re = f(Ge). The solid line is the actual function corresponding to C_{Ract}; the curves according to Equations (12) and (13) consist of dashed lines and dot-dash lines, respectively. If this relation is inserted in Equation (7) solved for d, the following will apply:

$$\text{I:}\quad d = \frac{\eta_A}{\rho_A \cdot v_A} \cdot \left[\left(\frac{2}{3} Ge\right)^2 - 4\right] = \frac{\eta_A}{\rho_A \cdot v_A} \cdot f_I(Ge) \tag{14}$$

$$\text{II:}\quad d = \frac{\eta_A}{\rho_A \cdot v_A} \cdot \left[20.(Ge - 10)\right] = \frac{\eta_A}{\rho_A \cdot v_A} \cdot f_{II}(Ge) \tag{15}$$

Through the introduction of the value Ge, i.e., the relation Re = f(Ge), these equations permit the direct determination of the theoretical droplet sizes.

4. Characteristics of a Jet Stream

/12

If the media, entry conditions, and ambient conditions are given, espcially those for the pneumatic atomization discussed here, the nozzle design plays the most important role. This is so not only insofar as the fineness of the droplets is concerned. The design of the nozzle affects also a number of characteristic jet properties which interact with each other. The jet characteristics are defined as follows:

1) Droplet size: diameter of spherical droplets;
2) Droplet size distribution: relations between droplet sizes and their frequency in the jet;
3) Jet uniformity or homogeneity: size range of droplets;
4) Jet concentration: local or integral relation between fuel volume and air volume in jet;
5) Fuel distribution: local fuel volume divided by [over] the jet cross section;
6) Jet configuration: geometric picture of nozzle jet (full cone, hollow cone, paraboloid, etc.);
7) Jet angle: angle between the jet tangents at the nozzle mouth;
8) Jet hardness: jet energy related to jet cross section;
9) Jet penetration depth: travel of droplets after they have

given off all of their kinetic energy to the surrounding air. This "actual penetration depth" is preferably expressed by means of its axial and radial components.

The relationships between these characteristics are extremely involved owing to reciprocal effects and cross effects: they cannot be given in any logical sequence. An attempt is nonetheless made to describe the most salient features in brief.

In the first place, the nozzle design directly affects the shape of the jet, the angle of the jet, and hardness of the jet. A fully conical jet with a low jet angle is very compact. The jet energy is concentrated in a relatively small volume, capable of attaining large penetration depth values. Under certain circumstances, however, there is a tendency to recombination. On the other hand, a hollow cone jet with high opening angle is relatively soft. More surrounding air is being encompassed, causing the jet to lose its energy at a rapid rate. Due to the greater working surface, the jet is better dissociated, better distributed in a combustion chamber, and better prepared for combustion. The jet angles increase with increasing surrounding air density, whereas increasing viscosity and density of the liquid /13 tend to decrease the jet angle. Such a change in the jet angle is accompanied by a change in droplet size in the opposite sense, which affects also the penetration depths: low jet angles and large droplets result in an increase of the penetration depth.

Jet uniformity and fuel distribution in the jet are also affected directly by the nozzle type. Fuel distribution improves (becomes smoother) with increasing distance from the nozzle as a consequence of turbulence. An increase in fuel viscosity and fuel density reduces the fuel distribution; increases in air density within the surrounding atmosphere improves it. Assuming we have the same average droplet size, a jet having high uniformity will be prepared (evaporated and brought to ignition temperature) faster than a jet with poor uniformity.

The penetration depths are influenced primarily by the jet configuration and, in turn, by nozzle design. In addition, the nozzle exit velocity also plays a role. The travel of the droplets in the jet within a specific period of time increases in the first section due to the increase in the exit velocity because this increases the exit impulse at a given flow rate. If the exit velocity increases, however, the droplet size decreases as shown in Equation (4). The jet of small droplets decelerates more rapidly owing to the surrounding air. This causes only a slight decrease in penetration depth in the overall sense. The effects of density increase in the surrounding air and of decrease in viscosity and density of the liquid are the same: the droplets will become smaller, the jet velocity will decrease at a faster rate, and the penetration depth will decrease.

To sum up, it may be said that a number of factors and their interaction must be considered in attempting to produce a nozzle jet with specific characteristics. Any solution can only be a compromise. Selection of the appropriate

jet depends on the combustion chamber size, combustion chamber configuration, and method of injection.

A number of penetration depth calculations for individual droplets have been reported in literature. However, the penetration depths of the entire jet are considerably greater than those of the individual droplets, since, in the case of a jet, the droplets exiting at the nozzle transfer their energy rapidly to the surrounding air in the beginning, and this factor causes a variation in the direction of the jet. Thus, the exiting droplets subsequently encounter less resistance and can therefore cover a many times longer path. The practical significance of the calculation or experimental determination of the penetration depths of individual droplets therefore appears to be not very great. According to Abramowitsch (Angewandte Gasdynamik [Applied Gas Dynamics], pp. 306-310) the jet of the duplex nozzles being discussed here can be considered as a gas jet containing heavy components (two-phase jet). This integral consideration of the nozzle jet appears to be closer to the realities of practical application and will therefore form the basis of the corresponding chapter of this report. /14

5. Design of Spray Diffusers

A number of nozzle designs (a total of 17) was developed in consideration of the parameters discussed in the introduction and on the basis of investigations conducted with them. The development and gradual improvement of these nozzles cannot be described in detail here. We will merely give a brief summary of the experiences gained with the various nozzles here; some conclusions will be made on the basis of the principles involved in the design. First, the following definitions are presented:

1a) Helical nozzles: spiral flow caused by helical grooves within the nozzle;
 b) Tangential nozzles: spiral flow caused by tangential fitting of the supply conduits;
2a) Small angle nozzles: jet angle $2\alpha_{jet} < 30°$;
 b) Wide angle nozzles: jet angle $2\alpha_{jet} > 90°$;
3a) Direct wide angle: widening of the jet by means of a Venturi fitting at strong exit twist (rounded exit instead of edged exit);
4a) Internal atomizing and acceleration: joining of the media and acceleration of the droplets within the nozzle;
 b) External atomizing and acceleration: joining of the media at the nozzle orifice, acceleration of the droplets outside;
5a) Double-flow nozzles: nozzles with one air flow and one liquid flow;
 b) Triple-flow nozzles: nozzles with two air flows and one liquid flow;
6) The means whereby the flows are combined at the nozzle orifice determine in triple-flow nozzles the following designations: parallel atomizer, two-stage atomizer, and reverse-flow atomizer.

The first nozzles were of the double-flow type with external atomization and acceleration. The axially flowing air was added to the liquid at the nozzle orifice radially, in one instance from the inside (internal supply) and in the

other instance from the outside (external supply). These radial supply nozzles /15
were very prone to blockage. The blockage phenomenon may have two basic causes. Here the effective mouth cross section of the first medium was reduced by the second medium, causing a throttling of the flowthrough of the latter (blockage effect, type A). In order to prevent this property, the subsequent nozzles were made with parallel supply. The prevailing nozzle velocity ratios $c_{air}/c_{fuel} \approx 20/1$ here reduced the relative velocities only very slightly. There was practically no deterioration of atomization quality.

Atomization and acceleration were practically transferred to the nozzle interior by fitting a cylindrical or slightly conical tube in front. This also made it possible to increase the hardness of the jet. It should be noted, however, that thick droplets developed at the jet boundary area owing to precipitation along the inside of the tube wall. This tendency became more pronounced if the twisting was increased. Whereas nozzles with external atomization cause the liquid to react to the surrounding pressure at the nozzle end as if it were a counterpressure, internal atomization nozzles require a higher liquid pressure at the nozzle intake since the air pressure acts as a counterpressure within the nozzle in this instance (blockage effect type B). Thus, the higher nozzle exit impulse is attained at the expense of somewhat more energy in internal atomization nozzles; however, such an arrangement could also facilitate a higher exit impulse in external atomizers. A suitable compromise was reached by only a slight backward shift (approximately 3-5 mm) of the mixing area into the nozzle interior (partly internal, partly external acceleration). The blockage effect and the tendency to precipitation could be kept within bounds by widening the channel first considerably and then slightly after the mixing area.

In the nozzles investigated here, conventional helical chambers were not considered. In these, the liquid flows into the nozzle from radial channels. This permitted the sizes of the double-flow versions to be kept very small (9 to 12 mm diameter for 250 to 300 liter/hr liquid). The helical effect was attained by a built-in helical groove or by the tangential fitting on the nozzle conduits. Tangential nozzles have smaller external dimensions than do corresponding helical nozzles, since the former have no helical grooves within the nozzle interior. It should be noted, however, that the type of torque production employed here have lower overall components and jet angles than did helical chamber nozzles. It was possible, nonetheless, to widen the jet by means of mushroom-shaped central bodies in front of the nozzle orifice or by means of a rounded constriction (to prevent detachment). Favorable curvature configuration of the Venturi fitting largely prevented precipitation. In double-flow nozzles, the air torque was directed opposite to that of the liquid. This is significant only with respect to its uniforming effect on the jet volume (elimination of symmetry). No effect on the quality of the atomization could /16
be observed (see above, velocity ratio). The air torque also makes the flow volume direction more uniform. Although it is possible to increase the jet angle by increasing the torque, the jet will become softer if this is done.

Since the degree of nozzle efficiency* in these very small double-flow nozzles is not very great, the next versions were built in sizes between 12 and 15 mm diameter. Double-flow reverse-flow atomizers were designed with D-11 and D-12 (see Figure 3a). Here the fuel is conducted through the internal nozzle tube into the enlarged mushroom, whence it is sprayed into the exiting air flow either through screened single holes (D-11) or through similarly screened ring slots (D-12) at an angle of approximately 180°. The two nozzles had some noteworthy characteristics: In the lower G_F region, the exiting air sucked the fuel in, in the medium range the nozzles showed no blocking tendency, and only in the high ranges of liquid throughput was there a slight indication of a blocking effect. Furthermore, the nozzle jet adjusts itself to the prevailing load: by increasing the fuel flowthrough, the jet angle was made larger (up to over 180°) so that ratio of local fuel amount to unit surface of jet cross section remained practically unchanged throughout the entire G_F operating range.

The two next nozzles (D-13 and D-14) were supposed to be experimental nozzles of universal character. Various types were made by simple unscrewing or replacement of nozzle components. In the D-13 the liquid flows through two rings with staggered holes toward the air or is sucked into the lower flowthrough range by the air. The total jet was very soft owing to excessively strong air torque, in spite of partial internal acceleration. A harder jet was realized with the D-14 version (see Figure 3b) owing to reduction of the torque (reduction of intake radius). The individual holes are replaced here by a ring slot. In order to make the exit flow uniform throughout the entire flow volume, a helical groove was incorporated in the fuel path. The version featuring the large mushroom (left, in picture) has a direct wide-angle character (hollow cone jet) featuring partly internal and partly external acceleration. The nozzle retained its wide-angle character even with the small mushroom (right, in picture) owing to the torque in the air; however, the jet became a full cone. Unscrewing of the screw cap at the nozzle mouth transformed the nozzle into a small-angle one by virtue of the exposed sharp exit edge.

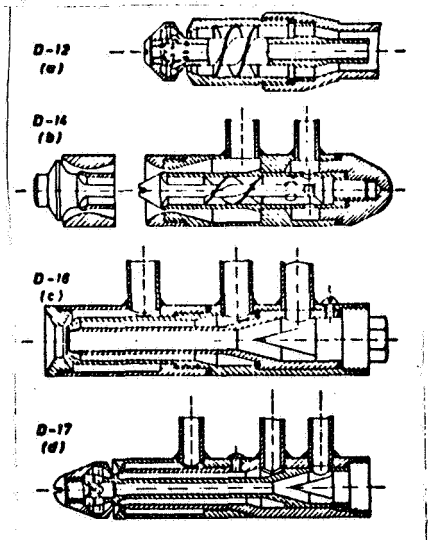

Figure 3

It was found that the most important point in nozzle design for attaining fine atomization is a relatively large contact surface between air and liquid at the mixing point that will be as big as possible, i.e., the volume-to-surface ratio for the liquid exit cross section (small hydraulic radius) should be as large as possible. This requirement can be met by subdividing the cross section into a number of individual holes or by designing it in the form of a ring slot. The version /17

*For definition, see section 7.1.3.

involving individual holes is simpler to manufacture not only because the operations of manufacture are less involved, but it also provides a somewhat smaller external nozzle diameter since no internal nozzle sleeve is required. A minor disadvantage of this solution is that the individual streams from the holes are visible in the total jet for a distance of approximately 10-20 mm. The ring slot configuration does not possess this disadvantage; however, it has somewhat larger external dimensions and imposes stricter requirements in terms of manufacturing precision. A small deviation suffices to make the narrow ring slot somewhat eccentric.

All nozzles described so far produced reasonably satisfactory atomization; however, jet uniformity was in most instances still somewhat unsatisfactory. The droplets were very small at the immediate contact surface between air and fuel (a few μ); however, the droplets were as large as up to 0.1 mm on the side of the fuel flow facing away from [opposite] the air.

In order to improve jet uniformity, nozzles with two air flows were constructed. In these triple-flow nozzle types, the air flows have opposite torque and these flows split the liquid ring from the inside and also from the outside surface. Very high relative velocities are obtained owing to opposing air torque even if the exit slits for the three flows are parallel (parallel atomizers). The torque equalizes itself after dissociation of the jet, causing it to become harder (torque compensation). Since the fuel velocity is very small compared to the air velocity, a liquid torque will not result in a significant increase in relative velocity and thus in atomizing quality. For the same reason, the in-flow angle of the liquid against the air (parallel supply, 90° supply or reverse flow supply) shows no noticeable changes in atomizing quality either. In triple-flow nozzles, there is an opportunity, however, to add the first air flow to the liquid and to blow off the already accelerated droplets in reverse-flow or back-twist fashion with the second air flow, causing a substantial droplet size decrease by secondary dissociation (two-stage atomizer). For all practical purposes, the sum of the two air velocities will be the relative velocity in this case. Equally good atomization will be attained if the two air flows are joined at an angle of close to 180° and if the liquid is added at the point of juncture along the angle bisecting line (reverse-flow atomizer). All of these triple-flow nozzles produced the expected improvement in jet uniformity, and they also caused a reduction in size of the average droplet diameter to about one half of that obtained with double-flow nozzles. /18

Triple-flow nozzle D-15 was to have a universal character, like nozzles D-13 and D-14. It can be described as an intermediate type between parallel and two-stage atomizers. Nozzle D-15 performed very well as a small angle nozzle. It was not suitable, however, in its wide-angle version with a mushroom shaped fitting because it was very difficult to manufacture. Thus, the triple-flow small- and wide-angle nozzles were constructed separately under the designation D-16 and D-17, respectively (see Figures 3c and 3d). This made it possible to keep the external nozzle diameters even smaller (16 mm for 250 to 300 liters/hr liquid). The back-twist of the air flows was created in both nozzles by tangential fitting of the intake conduits. The figure shows the conduits in the plane of the section. In D-16 the air flows meet at the mouth at an angle of 60° to each

other. The liquid is added between the two at an angle of 30°. The air twist is compensated after exit from the nozzle so that the jet becomes extremely hard, supported partly by internal acceleration. It is very finely atomized and has a good degree of uniformity.

In D-17, the torque of the internal air flow is practically entirely lost owing to the complicated path over the mushroom shaped fitting; however, this arrangement results in a uniform impact pattern on the exit ring slot. The two air flows meet at the mixing point at an angle of 150° to each other; the liquid flows in at an angle half of this. The effective exit angle of the ring slot leading from the mixing area to the outside is 60° to the nozzle axis, resulting in a jet angle of $2\alpha_{jet} = 120°$. Nozzle D-17 is principally /19
of the internal acceleration type. Thus the jet is relatively hard in spite of the angle characteristics and the very small size of the droplets. Depending on the operation point, nozzles D-16 and D-17 take in the liquid themselves or offer only a small blocking effect. These triple-flow versions marked the end of nozzle design here.

6. Energy Considerations

6.1 Theoretical Pressure Recovery

In the evaluation of the practical significance of pressure gas atomizing systems, the problems involving energy expenditure and possible pressure recovery are the most important ones. The use of the volumes or of the atomizing air ratio $\lambda_{AN} = G_{AAN}/G_F$ and the specific air volume $\ell_1 = G_{AAN}/G_{ACC}$ is not sufficient for the evaluation of the system.

Since the liquid only seemingly flows to the atomizing nozzles or since in some nozzle types it is propelled by jet suction effects, the temporal fuel energy in the cold test without combustion $E_F = G_F.H_F$ is negligible in these rough considerations compared to the energy of the atomizing air. Thus, the considerations presented here are also applicable to air injection for flame stabilization. In addition to the assumption that air is the sole energy carrier as it enters the nozzle, further permissible assumptions are made for the overall evaluation. These include the assumption that the gases involved are ideal and that state changes take place in an adiabatic manner. If the losses in the nozzle and the mixing chamber (combustion chamber) are not considered, the energy equation on the cold test without combustion can be rendered in the following manner:

$E_{AAN} + E_{ACC}$ entrance $= E_{GCC}$ exit or, with simplified indexes

$E_1 + E_2 = E_3$. By introducing the flowrates and enthalpies, we obtain:

$$G_1.i_{1t} + G_2.i_{2t} = (G_1 + G_2).i_{3t}$$

Transformations

$$1 + \frac{G_2}{G_1} = \frac{i_{1t} - i_{2t}}{i_{3t} - i_{2t}}$$

$$i_{1t} - i_{2t} = A \cdot R_2 \cdot T_{2t} \cdot \frac{\kappa_1}{\kappa_1 - 1}\left[\left(\frac{p_{1t}}{p_{2t}}\right)^{\frac{\kappa_1 - 1}{\kappa_1}} - 1\right]$$

$$i_{3t} - i_{2t} = A \cdot R_2 \cdot T_{2t} \cdot \frac{\kappa_3}{\kappa_3 - 1}\left[\left(\frac{p_{3t}}{p_{2t}}\right)^{\frac{\kappa_3 - 1}{\kappa_3}} - 1\right]$$

/20

$$1 + \frac{G_2}{G_1} = \frac{\frac{\kappa_1}{\kappa_1 - 1}\left[\left(\frac{p_{1t}}{p_{2st}} \cdot \frac{p_{2st}}{p_{2t}}\right)^{\frac{\kappa_1 - 1}{\kappa_1}} - 1\right]}{\frac{\kappa_3}{\kappa_3 - 1}\left[\left(\frac{p_{3t}}{p_{2t}}\right)^{\frac{\kappa_3 - 1}{\kappa_3}} - 1\right]}$$

Solving for p_{3t}/p_{2t} we get:

$$\frac{p_{3t}}{p_{2t}} = \left\{1 + \frac{\frac{\kappa_1}{\kappa_1 - 1}\left[\left(\frac{p_{1t}}{p_{2st}} \cdot \frac{p_{2st}}{p_{2t}}\right)^{\frac{\kappa_1 - 1}{\kappa_1}} - 1\right]}{\frac{\kappa_3}{\kappa_3 - 1} \cdot \left(1 + \frac{G_2}{G_1}\right)}\right\}^{\frac{\kappa_3}{\kappa_3 - 1}} \qquad (16)$$

At a mean combustion chamber intake Mach number $M_2 \approx 0.2$, corresponding to $p_{2st}/p_{2t} \approx 0.97$, a value of $\kappa_1 = \kappa_A = 1.4$ and $\kappa_3 = \kappa_G = 1.33$, the theoretical recoveries p_{3t}/p_{2t} for a series of injection pressure conditions $\pi_{AN} = p_{1t}/p_{2st}$ and relative injection quantities (air expenditure) $\ell_1 = G_1/G_2$ are shown in Figure 4.

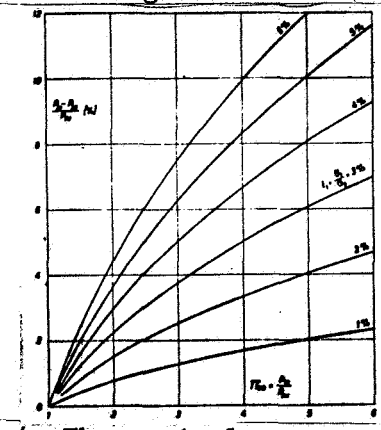

Figure 4. Theoretical pressure recovery with air injection (free of losses)

The curves appear very promising; a mean air expenditure of 2 to 3% provides theoretically with average nozzle pressure ratios of 3 to 4, roughly 3 to 5% increase in total pressure in the combustion chamber. Let us investigate briefly what amount of this is actually recoverable.

6.2 Actual Pressure Recovery

If we consider the losses in the nozzle by means of the nozzle efficiency η_N and the losses caused by turbulent mixing of the jet with the air in the chamber by means of a mixing effectiveness, η_M, and if we insert these efficiency figures into the above recovery formula Equation (16), we get the following:

$$\frac{p_{3t}}{p_{2t}} = \left\{ 1 + \frac{\frac{\varkappa_1}{\varkappa_1 - 1} \cdot \eta_N \cdot \eta_M}{\frac{\varkappa_3}{\varkappa_3 - 1} \cdot \left(1 + \frac{G_2}{G_1}\right)} \left[\left(\frac{p_{1t}}{p_{2st}} \cdot \frac{p_{2st}}{p_{2t}} \right)^{\frac{\varkappa_1 - 1}{\varkappa_1}} - 1 \right] \right\}^{\frac{\varkappa_3}{\varkappa_3 - 1}} \qquad (17)$$

To estimate the efficiency studies by Weydanz (Die Vorgänge in Strahlapparaten) [The Processes in Jet Systems] and studies of this author were used. Weydanz obtained efficiencies for injector nozzle values between 80 and 40% (depending on nozzle pressure ratio. The author's studies for the nozzles used here gave η_N values between 30 and 70%, with values between 30 and 50% for very small nozzles, and values between 50 and 70% for somewhat larger nozzles.

The mixing area efficiency values according to Weydanz depend on velocity relations, mass relations, and mixing chamber sizes. Since the mixing chamber (the combustion chamber) available here does not have the optimum configuration with respect to η_N, mixing effectiveness values between 5 and 15% are obtained for the prevailing velocity and mass relations. Thus, values of $\eta_N \cdot \eta_M \approx 0.5 \cdot 0.1 = 0.05$ may be used as average. If this value is inserted into the recovery formula Equation (17), the ordinate scale in Figure 4 will change by about one power of ten; thus, actual recoveries of 0.5% may be expected, at best. The injection energy thus becomes almost entirely lost and it is therefore not possible to talk about effective pressure recovery. It is possible to draw important conclusions regarding the permissible energy expenditure in air injection. /21

6.3 Permissible Energy Expenditure in Case of Air Injection

The loss of almost the entire injection energy established on the basis of an overall calculation in the preceding section makes it necessary to set up the maximum permissible energy expenditure as the value corresponding to the usual pressure injection of the fuel. If, in case of pressure injection, the injection output is $E^{*} = G_F \cdot H_F^{*}$ kgm/sec , and in case of compressed gas atomization it is $E = G_F \cdot H_F + G_A \cdot H_A$, the condition $H_F^{*} = H_A \cdot G_A/G_F = H_F + \lambda_{AN} \cdot H_A$ must be fulfilled for the same specific energy expenditure $E^{*}/G_F = E/G_F$, or else

$$\frac{H_F^{*}}{H_A} = \frac{H_F}{H_A} + \lambda_{AN} \qquad (18)$$

The heads H_F and H_A prevailing at the pressures employed here give us a ratio with values between 0.0010 and 0.0025. Thus, one may disregard the ratio H_F/H_A with respect to λ_{AN} ($\simeq$ 0.4 to 0.6) in the first approximation for the estimation of the head ratio H_F^*/H_A^* using Equation (18); then the relation $H_F^* = \lambda_{AN} \cdot H_A$ is obtained as the requirement for the same specific energy expenditure E/G_F in case of pressure gas atomization and pressure injection.

Similar requirements for the permissible energy expenditure apply for /22
the use of air jets for flame stabilization, since practically no energy or pressure recovery may be expected. The permissible energy expenditure will be determined in these instances by the pressure losses or the loss value H_{LFH} which would be given by mechanical interference flameholders:

$$E_{Perm} = G_{AAN} \cdot H_{AAD} = G_{ACC} \cdot H_{LFH}; \quad \frac{H_{AAN}}{H_{Evap}} = \frac{H_{LFH}/H_{Evap}}{G_{AAN}/H_{ACC}} \qquad (19)$$

At a 4% mean relative loss value H_{LHF}/H_{Evap} and an air expenditure of, for example, 2% (G_{AAN}/G_{ACC}), an injection head equalling twice the compression transfer level is permissible according to Equation (19). Under normal circumstances, however, considerably lower values would suffice. One may presumably expect significant energy savings if the air-fuel jets are directly employed for flame stabilization. It has not been possible to include this problem into the scope of the present project.

7. Experimental Investigation of the Relations Between Jet Parameters and Penetration Depths

7.1 Jet Parameters (Nozzle Performance Charts)

7.1.1. Flow Rate Performance Charts

Water was used as the liquid for the nozzle and jet investigations. It was obtained from the water supply network and piped to the nozzles through a pressure regulator and a ROTA flowmeter. The atomizing air is fed to a pressurized container by a piston compressor. From there, it is piped to the nozzle through a pressure regulator and a diaphragm measuring section.

The flow rate performance graphs of the nozzles represent the relations between the flow rates and pressures, and also the mutual effects of liquid and atomizing air. The following two figures (Figures 5 and 6) show, as examples, the flow rate performance graphs for D-14 and D-17. The pressures p_{A3t} and p_{W3t} are measured immediately before the nozzle (intake pressures). The characteristic curve for water flow rate $G_W = f(p_{W3t})$ is only slightly affected by the air

pressure in nozzles D-14, D-13, and D-13S. The blockage effect of air upon water does not follow the increase in air pressure in a consistent manner: it shows a variable tendency. In the lower G_W range, the nozzles exhibit a suction effect, i.e., the air transports 50 to 100 kg liquid/hr owing to an ejector effect (see Figure 5a). The suction effect is small (up to $G_W \approx 30$) in nozzles D-17, D-16, D-15, and D-12. In these cases the flowthrough curves shift with increasing p_{A3t} practically without a trend reversion (see Figure 6a). The water flow rate performances play no role in subsequent investigations since, as has been shown in the preceding chapter, the liquid energy is negligible compared to the air energy. The air flow rate performance graphs, however, do become important to the impulse performance graphs, though the blockage effect of water upon air mostly is not very great. Figures 5b and 6b show the air performance in the form of $G_A = f(G_W)$ with p_{A3t} as the characteristic value for nozzles D-14 and D-17, since this way of rendering makes the blockage effect most clearly apparent. In this representation, the curves appear nearly as clusters of straight lines. The superimposed (dashed line) rendering of $\Delta G_A/G_{Ao}$ against G_W with p_{A3t} as the characteristic value shows, however, different courses (G_{Ao} = air flow rate when $G_W = 0$).

/ 23

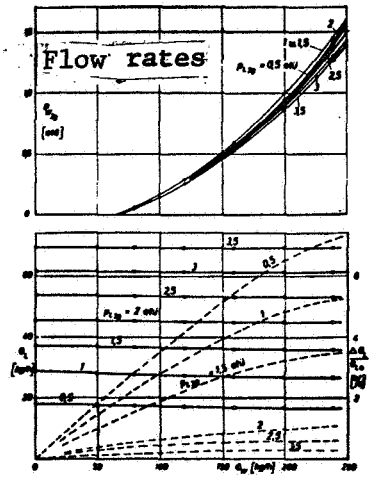

a

atü = gauge atı
[ato]

b

Figure 5

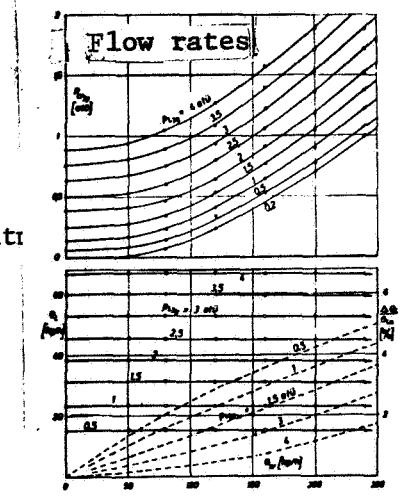

Figure 6

Two types of blockage may be distinguished:

a) The blockage at low G_{Ao} values, ΔG_A, first increases with increasing values of p_{A3t}, then decreases and attains nearly the value of zero (example: D-14, Figure 7a).
b) The ΔG_A values remain approximately constant during increase at constant G_W values in relation to p_{A3t} (example: D-17, Figure 7b).

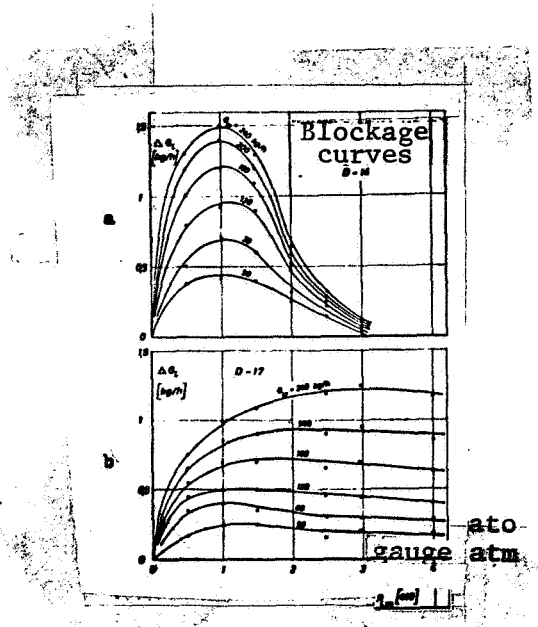

Figure 7

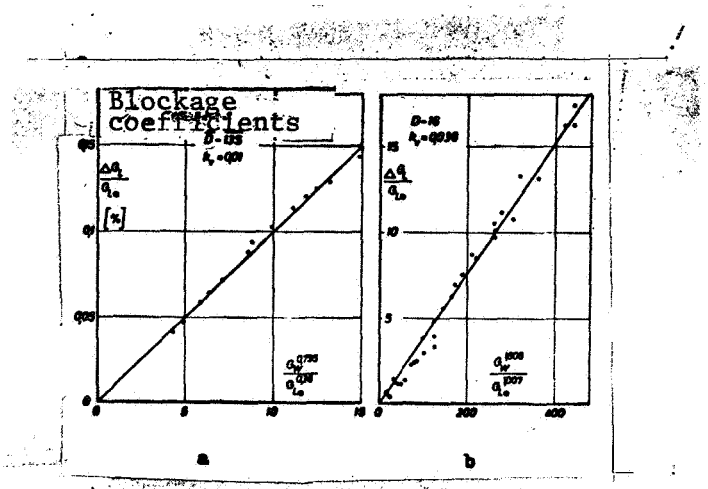

Figure 8

Nozzles D-12 and D-13 also belong to a); nozzles D-13S, D-15 and D-16 also belong to b).

Various assumptions were made to enable the mathematical characterization of the blockage. On a purely empirical basis, the best correlations with experimental results were obtained by the relation /24

$$\frac{\Delta G_A}{G_{Ao}} = k_B \cdot \frac{G_W^r}{G_{Ao}^s} \qquad (20)$$

where k_B, r, and s represent the blockage coefficients of the nozzles. They were obtained by means of logarithmic plotting (examples: D-13S and D-16; see Figure 8).

It is apparent that the different blockage curves are reflected by the s/r ratios. For type a, $s/r > 1$; for type b, $s/r < 1$. The magnitude of the blockage may be characterized for type a both by s and by k_B: High k_B values indicate high blockage; high s values indicate low blockage. For types b, the blockage coefficients alone do not indicate the magnitude of the blockage.

The linear expression $\Delta G_A/G_{Ao} = k_{Bmax} \cdot G_W/G_A$, where k_{Bmax} represents the maximum blockage in the nozzle operating range, sufficiently accurate for a rough estimate of the blockage. The values for k_{Bmax} are obtained, by plotting $\Delta G_A/G_{Ao}$ against G_W/G_A, as tangents, to the curves, showing the maximum rise from the zero point. According to the k_{Bmax} values (see Table below), nozzles D-15, D-16, and D-12 have high blockage tendencies ($k_{Bmax} > 1$); /25 nozzles D-14, D-17, and D-13 have medium blockage tendencies ($0.1 < k_{Bmax} < 1$); and nozzle D-13S has a low blockage tendency ($k_{Bmax} < 0.1$). Since the impulse performances of the nozzles to be discussed in the next chapter are very sensitive to incorrect adjustment of blockage, the diagrams for these will be

based on the measured flow rate performance.

Type	Nozzle	k_B	r	s	s/r	k_{Bmax}
a	D-12	11.4	0.995	1.642	1.652	1.1
	D-13	0.0045	0.731	3.87	5.295	0.4
	D-14	0.018	0.668	2.87	4.3	0.7
b	D-13S	0.01	0.795	0.38	0.478	0.03
	D-15	2.2	0.66	0.5	0.758	2.7
	D-16	0.038	1.808	1.007	0.557	2.4
	D-17	0.15	1.22	1.001	0.824	0.5

7.1.2 Nozzle Velocity Head Performance Graphs

The primary factors affecting the penetration depth (range) of jets are, in addition to the ambient effects (such as density and velocity of the surrounding air), the energies and velocity heads present in the jets. One should expect that a comparative evaluation of the jet parameters (velocity, velocity head, energy, angle, etc.) together with the penetration depths to be investigated and deviations in the blow deflection of the jets at various angles would lead to certain relationships. To make this comparison, the nozzle velocity head performance graphs were determined.

The axial velocity heads were determined by means of measuring the jet recoil. In the velocity head measurements, the nozzle was placed within a receptacle fitted on a hydraulic thrust gauge. This gauge contained a set of resistance-measuring expansion strips in temperature-compensated circuits. The transmitter was located in one branch of a measuring bridge. The measurements were performed with a jet flowing downward vertically. The weights of the nozzle and of the receiver were compensated by means of an adjustable spring and set to [adjusted for] zero on the bridge.

In these tests the nozzles were operated first with air alone and they were then studied for relative velocity head changes by the addition of water. The measured axial air velocity head together with the jet angles characterize the actual [meridian] velocity head: $I_m = I_{ax}/\cos \alpha_{jet}$. The sketch in Figure 9 shows the components and designations used.

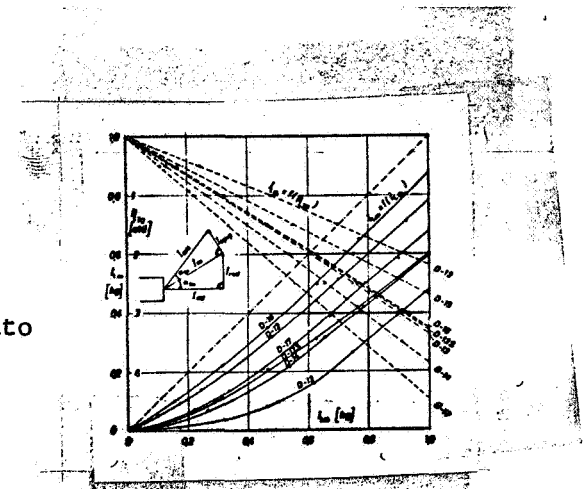

Figure 9

ato

The upper triangle formed by I_m, I_{tan}, and I_{act} is rotated 90° around the plane of the drawing. In order to determine the jet angle, a very small amount of water, barely visible with the naked eye, has been added to the air, and the effect was photographed over very long exposure periods. The evaluation of the photographs showed that the jet angles for the narrow jet nozzles D-15, D-13S, and D-16 were $2\alpha_{jet} \approx$ ≈ 20°, whereas in case of the wide-angle nozzles the mushroom angle, or the exit slot angle, represented the jet angle. /26

The theoretical air momentum I_{Ath} may be determined for the individual nozzles from the flow rate performance graphs. The following equation applies:

$$I_{Ath} = \frac{G_A}{g} \cdot o_{Ath} = \frac{G_A}{g} \cdot \sqrt{2t.H_A} \qquad (21)$$

If $G_A = f_1(p_{A3t})$ and $H_A = f_2(p_{A3t})$, I_{Ath} will equal $f_3(p_{A3t}$ upon expansion into the free atmosphere (counterpressure p_a is unchanged). The upper curve cluster (dashed line) in Figure 9 represents the relations between I_{Ath} and p_{A3t} for the nozzles investigated. This is a cluster of almost straight lines. The other curve cluster (solid line) in this figure represents the relations between the measured air meridian impulses and the theoretical air impulses. The deviations of these curves from the 45° line may be explained not only by nozzle losses but also by the fact that certain of the twist components of the jets were not taken into consideration. By assuming approximately the same losses in all nozzles, it becomes possible to estimate the approximate jet twist that results. The lowermost curve of this figure (D-13) has the strongest twist; the uppermost (D-16), the weakest.

The question now arises whether this air velocity head performance could be generalized, i.e., whether an expression could be introduced for it with which all nozzles would give the same curve. The solution has been found in the form of

$$\frac{I_{Am}}{I_{Ath}} = K_N^i \qquad (22)$$

where K_N represents a nozzle constant and $i = f(I_{Ath})$ the air impulse exponent. In the upper portion of Figure 10, 1/i was plotted against I_{Ath} with the expectation that the relation will be linear. However, a slightly curved

line was obtained. Logarithmic plotting yielded for the measured values the following expression:

$$\frac{1}{i} = 0.629.(I_{Ath} + 0,05)^{1.13} + 0,15 \qquad (23)$$ /27

The course of i was also inserted in the upper portion of Figure 10. The lower portion of Figure 10 provides proof of the validity of Equations (22) and (23): The plotting of I_{Am}/I_{Ath} against K_N^i gives for all nozzles a straight line inclined at a 45° angle. The nozzle constants K_N are given in Figure 12 together with other nozzle parameters.

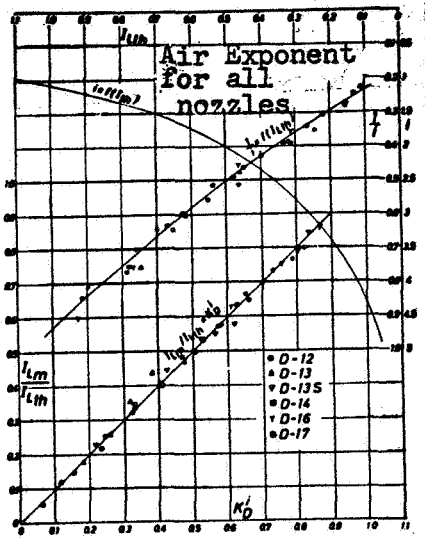

Figure 10

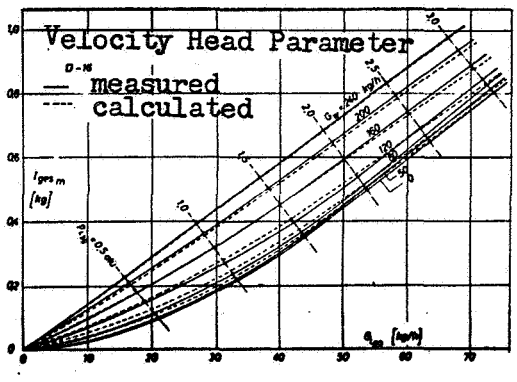

Figure 11

The velocity heads with air and liquid (subscript tot) in the jet were measured in a similar manner as was the air impulse. In these measurements, the values of p_{A3t} and G_W were varied in a systematic manner. The meridian velocity heads $I_{tot\ m}$, calculated from the values of $I_{tot\ ax}$ and the jet angles α_{jet} are presented in Figure 11 for the example of D-16 (solid line). The cluster of dotted line curves in Figure 11 should be disregarded for the present.

The increases in the values of the impulse with increasing values of G_W show different trends depending on the nozzle and on the G_A range (progressively or degressively rising). The inclination of the p_{A3t} lines in these velocity head parameters again gives the magnitude of the blockage. Basically, all diagrams appear the same or very similar. One may thus hope that general relations and performances can be derived here too. The best way to do this was to introduce a fictive velocity, c_{fm}, defining the impulse rate at the nozzle mouth. This fictive velocity is defined by the following expression:

$$I_{tot_m} = \frac{G_A + G_W}{g} \cdot c_{fm} = \left(1 + \frac{G_W}{G_A}\right) \cdot \frac{G_A}{g} \cdot c_{fm} \qquad (24)$$

/28

The following equation is obtained by dividing Equation (24) by $I_{Am} \cdot G_A/g$:

$$\frac{I_{tot_m}}{I_{Am}} = \left(1 + \frac{G_W}{G_A}\right) \cdot \frac{c_{fm}}{c_{Am}} \qquad (25)$$

The relative impulse increase $I_{tot\ m}/I_{Am}$ can be determined from this equation if it is possible to render a conclusion regarding the velocity ratio c_{fm}/c_{Am}. It is evident that here, too, a power relation,

$$\frac{c_{fm}}{c_{Am}} = K_F \cdot \frac{G_A^n}{G_W^m} \qquad (26)$$

represents the situation quite adequately. This expression is no longer valid. Only in case of very small water throughputs outside of the operational range (where $G_W \to 0$). The range within which the expression is valid can be established by the requirements $G_W/G_{Wmax} >> 1/10$, and $c_{fm}/c_{Am} << 0.8$. There is a further requirement, namely c_{Am} or p_{A3t} must be constant. This brings in the blockage characteristic here (changes in the value of G_A through G_W where p_{A3t} is constant). The values of the exponents n and m are found by logarithmic plotting. The c_{fm}/c_{Am} against G_A^n/G_W^m plot (see Figure 12), together with the inclinations of the lines, gives the nozzle figures K_F (constants of the fictive jet velocity). The cluster of curves drawn in dashed lines in Figure 11 represents the impulse parameter for D-16 together with the values established for K_F, n, and m. The correlation between these calculated curves and the measured curves may be called satisfactory. The same also applies to the other nozzles.

The question now arises whether there exists a relation between the various velocity head indexes. In order to answer this question, the values of n and K_F were first plotted against the value of K_N (Figure 13, right side). As can be seen, curves may be drawn through each of seven points (nozzles) which show hardly any scatter. The G_W exponent m, which could not initially be fitted, eventually also provided a curve with the aid of auxiliary plotting $(n + K_F/10)$; however, this curve exhibited a degree of scatter (see left side in Figure 13).

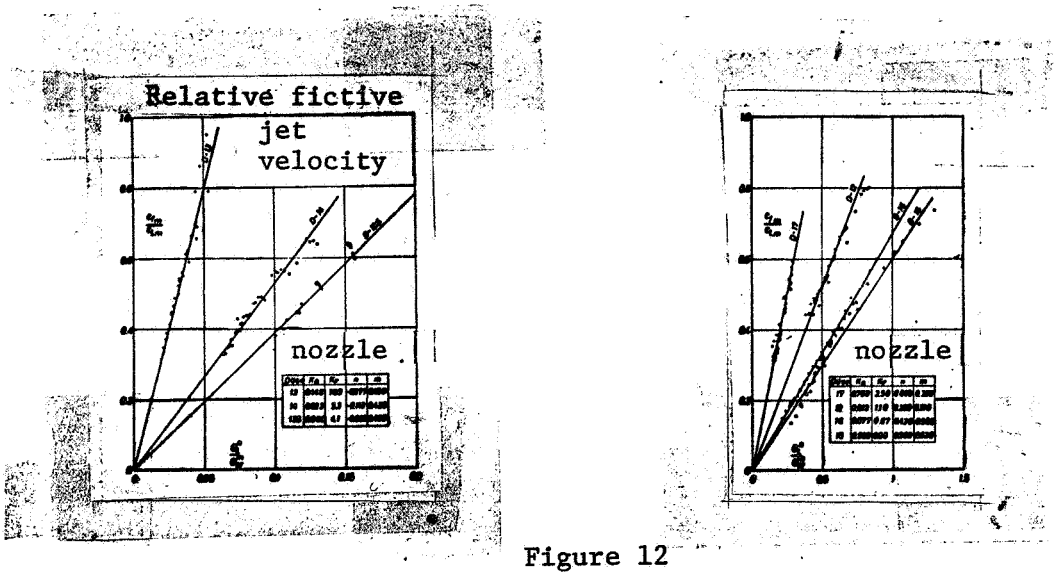

Figure 12

Relation of the nozzle figures

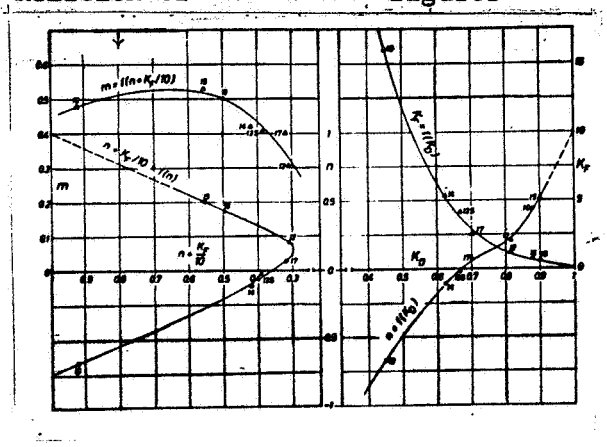

Figure 13

Although no theoretical foundation has been found for the relations established in this manner, the relationships presented in diagrams permit an advance determination of the velocity head performances. Uncertainties are caused first of all by the assumption of the nature of blockage and the value of K_N for a specific type of nozzle. If a prototype of the nozzle involved is made, simple measurements of its flowthrough characteristics will clarify these uncertainties and it will be possible to establish the more difficult to measure velocity head performance on the basis of the air flow rate performance. /29

7.1.3. Nozzle Efficiency

The energy present in the nozzle jet, $E_{\text{tot act}}$, together with the value of the nozzle intake energy, $E_{\text{tot th}}$, provides the definition of the nozzle efficiency:

$$\eta_N = \frac{\text{Energy of the nozzle jet}}{\text{Nozzle intake energy}} = \frac{E_{tot\ act}}{E_{tot\ th}} \qquad (27)$$

The temporal intake energy is composed of $E_{Ath} = G_A \cdot H_A$ and $E_{Wth} = G_W \cdot H_W$.

The sum is $E_{tot\,th} = E_{Ath} + E_{Wth} = G_A \cdot H_A + G_W \cdot H_W = G_A \cdot H_A \cdot (1 + \frac{G_W}{G_A} \cdot \frac{H_W}{H_A})$

As has been the case with the energy consideration (Chapter 6), the bracketed expression is practically unity since $H_A >> H_W$; thus,

$$E_{tot\,th} \approx G_A \cdot H_A \qquad (28)$$

The temporal jet energy can be determined from the values of impulse and flow-through. Generally:

$$I = \frac{Q}{g} \cdot c \quad \text{or} \quad c = I \cdot \frac{g}{Q} \text{ and } E = I \cdot \frac{c}{2} \quad \text{or} \quad E = \frac{g}{2} \cdot \frac{I^2}{Q} \cdot$$

/30

The following is obtained for the present case:

$$E_{tot\ act} = \frac{g}{2} \cdot \frac{I^2_{tot\ act}}{(G_A + G_W)} \qquad (29)$$

The total impulse, $I_{tot\ act}$, can be calculated from the measured axial impulse, the jet angle, and the torque angle:

$$I_{tot\ act} = \frac{I_{tot\,ax}}{\cos \alpha_{jet} \cdot \cos \alpha_{Tq}} = \frac{I_{tot\,m}}{\cos \alpha_{Tq}}$$

Thus,

$$E_{tot\ act} = \frac{g}{2} \cdot \frac{1}{(G_A + G_W) \cdot \cos^2 \alpha_{Tq}} \cdot I^2_{tot\,m}$$

or

$$E_{tot\ act} = \frac{g}{2} \cdot \frac{1}{(G_A + G_W) \cdot \cos^2 \alpha_{Tq}} \cdot \left(\frac{I_{tot\,m}}{I_{Am}}\right)^2 \cdot \left(\frac{I_{Am}}{I_{Ath}}\right)^2 \cdot I^2_{Ath} \qquad (30)$$

If we combine with this Equations (22), (25), and (26), and also the expression $I_{Ath} = G_A \cdot \sqrt{2H_A/g}$, we obtain the following:

$$E_{tot\ act} = \frac{G_A \cdot H_A}{\cos^2 \alpha_{Tq}} \cdot (1 + \frac{G_W}{G_A}) \cdot (K_N^1 \cdot K_F \cdot \frac{G_A^n}{G_W^m})^2 \qquad (31)$$

If we insert the two energies according to Equations (28) and (31) in the

effectiveness Equation (27), we obtain the following:

$$\eta_N = (1 + \frac{G_W}{G_A}) \cdot (\frac{K_N^i \cdot K_F}{\cos \alpha_{Tq}} \cdot \frac{G_A^n}{G_W^m})^2 \quad (32)$$

Since the nozzle constant K_N defines the values of K_F, n, and m (see Figure 13), the value of η_N will depend on the nozzle, on the throughputs, and on the exponents $i = f(I_{Ath})$ or $f(p_{A3t})$. The relation between I_{Ath} and p_{A3t}, however, is also dependent on the nozzle (see Figure 9). It has been mentioned earlier that Equation (26) does not apply when $G_W \to 0$. For this case, $c_{fm}/c_{Am} \to 1$. If the nozzle is charged with air only, the following equation will apply:

$$\eta_{NL} = (\frac{K_N^i}{\cos \alpha_{Tq}})^2 \quad (33)$$

In the subsequent penetration depth investigations it was established that the axial and radial impulse components are the principal determining factors. For the advance determination of the attainable penetration depths, therefore, it is also necessary to know the impulse values prevailing in the axial or meridian section of the nozzle, whereas the overall components have a lesser degree of significance. In order to establish the meridian plane impulses, a nozzle meridian efficiency value (η_{Nm}) is introduced. It is defined according to Equations (32) or (33) by means of the following expression:

$$\eta_{Nm} = \eta_N \cdot \cos^2 \alpha_{Tq} \quad (34)$$ /31

This involves the effectiveness for the peripheral components that were not considered. Figure 14 shows the η_{Nm} values of the nozzles investigated plotted against I_{Ath} for the case where $G_W = 0$. The strong-twist nozzles D-13, D-13S, and D-14 are placed quite low, as expected. Attempts were made to measure the torque angle of the nozzles in operation without water with the aid of a miniature probe (1 mm diameter) in a special holder, in order to be able to establish the values of η_N. For example, D-13S gave a value of 48.5° for the torque angle; D-14, a value of 33.3°. Thus, the η_{Nm} values for these nozzles increase by the factor of $1/\cos^2 \alpha_{Tq} = 2.28$ or 1.43 to the value of η_N.

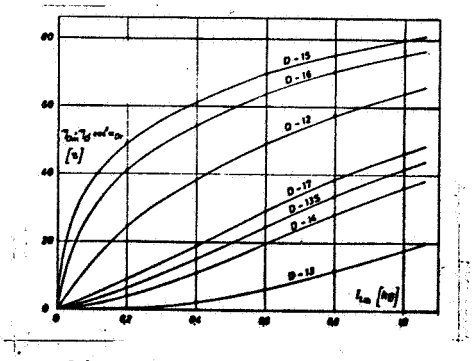

Figure 14. Nozzle efficiency curves (no allowance is made for peripheral components, no liquid used).

The efficiency curves (without liquid) represented are maximum values. If water is added, the expression $K_F \cdot G_A^n / G_W^m = c_{fm}/c_{Am}$

in Equation (32) will become smaller than one and quadratically affect the efficiency, whereas the member $(1 + G_W/G_A)$ will become greater than one but will act linearly only here.

7.1.4. Jet angle (D-12)

Nozzle D-12 assumes a special position among the nozzles investigated owing to its jet angle. Whereas the other nozzles show a practically unchanged jet angle over the entire operational range, nozzle D-12 adapts its jet angle to the prevailing load, i.e., the jet angle increases with increasing values of G_W. Additional variations in the jet angle can be induced by fitting a mushroom angle which further widens the range. In order to investigate the relationship, nozzle D-12 was fitted with a series of exchangeable mushroom fittings having different angles (α_M = 0°, 15°, 30°, 45°, 60°). The jet angles at various G_A and G_W values were photographically determined. Figure 15 shows the measured (half) jet angles α_{jet} for α_M = 30° (solid lines).

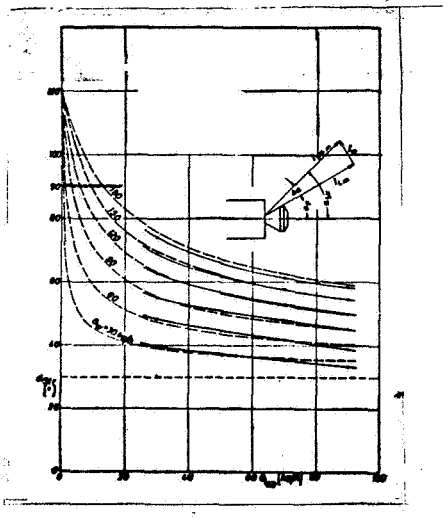

Nozzle D-12, α_M = 30°
Variation of the jet angles with throughputs
—— measured
- - - calculated
α_{jet} = half jet angle

Figure 15

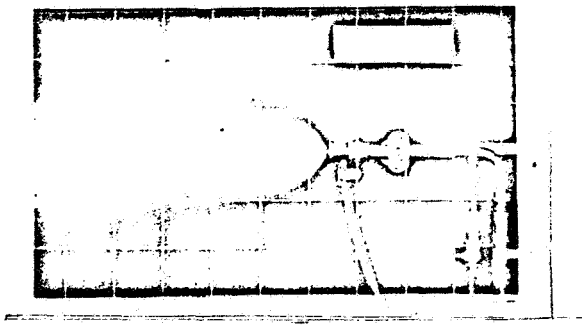

Figure 16

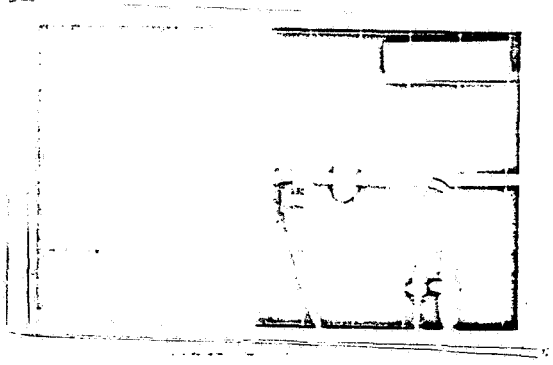

Figure 17

Attempts were then made to derive an expression for the characterization of the jet angle as a function of nozzle throughputs G_A and G_W, to permit the advance determination of the jet angle for this type of nozzle. The following expressions can be established on the basis of the sketch in Figure 15:

$$\alpha_{jet} = \alpha_M + \Delta\alpha$$

$$\cos \Delta\alpha = I_{Am}/I_{tot\ m}$$

This shows once more that in operation with air only, the jet angle is the same as the mushroom angle. If the general impulse relations discussed in 7.1.2 are inserted in Equations (25) and (26), the following equation is obtained:

$$\frac{1}{\cos \Delta\alpha} = \left(1 + \frac{G_W}{G_A}\right) \cdot K_F \cdot \frac{G_A^n}{G_W^m} \qquad (35)$$

Although the jet angles established with the aid of this equation show the real tendencies, their numerical value is too high. The following explanation was established for this phenomenon: Immediately behind the nozzle mouth there is another air flow above the jet contour determined by the droplet paths. This additional flow becomes mixed thoroughly with the droplets only at a distance of approximately 10 cm behind the nozzle mouth (see Figure 16). This superimposed air flow has the greater $\Delta\alpha$ values according to the above calculation. The measured jet angles (jet tangent at the nozzle mouth) are somewhat smaller than the values calculated from the impulses. After a number of modifications, the following impulse factor was found to be quite useful:

$$\frac{1}{\cos \Delta\alpha} = \frac{c_{Am} \cdot G_A + c_W \cdot G_W}{c_{Am} \cdot G_A} = 1 + \frac{c_W \cdot G_W}{c_{Am} \cdot G_A} \qquad (36)$$

If one assumes that at constant values of G_W the velocity c_W will increase linearly with the air velocity, the following equations will apply: /33

$$c_W/G_W = K_\alpha \cdot c_{Am} \qquad \text{or} \qquad c_W/c_{Am} = K_\alpha \cdot G_W$$

Insertion into Equation (36) gives the following:

$$\frac{1}{\cos \Delta\alpha} = 1 + K_\alpha \cdot \frac{G_W^2}{G_A} \qquad (37)$$

This equation gives good correlation with experimentally determined values for all mushroom angles (compare the cluster of dotted line curves in Figure 15). The jet angle coefficient K_α, varies to some degree with the mushroom angle:

$$K_\alpha = 10^{-4} \cdot \left(5 - \frac{\alpha_M}{30}\right) \qquad (38)$$

with a large mushroom angle value (for example, 50 to 60°) this nozzle D-12 permits jet angles of up to $2\alpha_{jet} = 180°$ (see Figure 17) or even higher (tipping or tilting of jet), depending on the operating point.

7.2. Penetration Depths (Jet Contours)

7.2.1. Measuring Section, Method, and Accuracy

In order to derive relations between the velocity heads and flow rates, on the one hand, and the penetration depths and deviations, on the other hand, the contours of the nozzle jets were photographed while being blasted with flows of various velocities and of various angles. These jet investigations were performed in a measuring section installed after the combustion chamber. In the cold test (atomization of water) the nozzle jets were first blasted with the cold combustion-chamber air stream. The velocity profile at the combustion chamber exit, except for a thin boundary layer, is practically constant throughout the torque tube cross section (see Figure 18). In order to prevent a significant decrease of the velocity and a change in profile throughout a suitable measuring length of approximately one meter, the exiting free air jet was placed between two parallel plates. In this manner it was possible to keep the measuring plane (middle section vertical to the plates) constant with respect to the profile and velocity. The photographs were taken perpendicular to the measuring plane.

Velocity profile in the cold measuring section
a = distance from the measuring section entrance

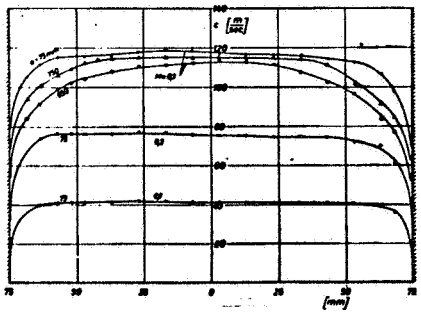

width of measuring section

Figure 18

In the first trial photographs, in front of a black screen, the jet was quite visible in the vicinity of the nozzle; however, the boundaries were so blurred at a somewhat greater distance from the nozzle that it was difficult to locate the jet contours precisely. In order to increase the contrast between jet and background, the latter was built in the form of an open cabinet with the opening in the front, covered on the inside with black velvet. A square velvet diaphragm before the measuring section also contributed to the elimination of light reflections. With the aid of these measures it was possible largely to eliminate any disturbing stray light from the camera. To increase the contrast further, we overexposed intensively and the films were developed very hard. A projector, whose sharply collimated light beam was concentrated as much as possible on the nozzle jet, served as the light source. Further inaccuracies are introduced by the nozzle operating points themselves. Small quantities of liquid give blurred contours owing to the tendency of the black background to be seen through the jet. The exposure times also influence

/34

the photographed jet boundaries. Longer exposure times result in somewhat larger penetration depths in the plotting.

The jet images were projected with the aid of a PHYWE microfilm reading device in a 1:1 scale onto a foundation and traced by hand in a coordinate system. Always the outermost, still visible droplet paths were taken as the jet contour. In spite of the precautionary measures described above, it was not possible to eliminate blurred views in areas distant from the nozzle; thus, all evaluations must be considered as being somewhat subjective. All these inaccuracies affecting the measurements result in errors in the penetration depth values and jet contours in the order of magnitude of approximately 10%. In spite of this factor, it is likely that the investigations performed provide data on the combustion chamber configuration and the installation of the nozzles and flameholders.

The approach flow velocities or Mach numbers for the investigation of the jet deformations can be established by means of the thrust measuring installation of the combustion chamber in a relatively easy manner (subscript 5 represents combustion chamber exit): By inserting into the thrust equation $S = c_5 \cdot G_5/g$ the throughput from the continuity equation $G_5 = F_5 \cdot \gamma_5 \cdot c_5$, the following expression will be obtained:

$$S = \frac{c_5 \cdot G_5}{g} = \frac{p_5}{g} \cdot \gamma_5 \cdot c_5^2 = 2 \cdot F_5 \cdot p_{5dyn} \qquad (39)$$

With the value of γ_5 from the gas equation, $c_5/c_{5cr} = M_5$, and $c_{5cr} = \sqrt{kgRT_{5st}}$, the following equation will apply:

$$S = F_5 \cdot p_{5st} \cdot \varkappa \cdot M_5^2 \qquad (40)$$

Equation (39) furnishes the mean velocity c_5, Equation (40) the mean Mach number M_5. Let us state here briefly in advance that these expressions also permit the determination of the flow rate for the combustion chamber. If c_5, rather than G_5, is replaced in the thrust equation from the continuity equation, a very precise throughput equation is obtained: /35

$$S = \frac{c_5 \cdot G_5}{g} = \frac{G_5}{g} \cdot \frac{G_5}{F_5 \cdot \gamma_5} \quad \text{or} \quad G_5^2 = \frac{g \cdot F_5}{R} \cdot S \cdot \frac{p_{5st}}{T_{5st}} \qquad (41)$$

It should be noted, however, that these expressions are valid only in the cold test owing to the factor T_{5st}; they nonetheless make a calibration of the combustion chamber intake measuring section possible.

7.2.2. Jet contours in the case of Parallel stream Injection

To investigate the jet contours in the case of parallel stream injection, the available wide angle nozzles (D-17, D-14, and D-12 with the large mushroom)

were fitted into the front part of the measuring section. Figure 19 shows an excerpt of the contours obtained. Figure 20 is a jet image from a nozzle operating point (D-17; G_W = 160 kg/hr; p_{A3t} = 2.5 ato; M = 0.2).

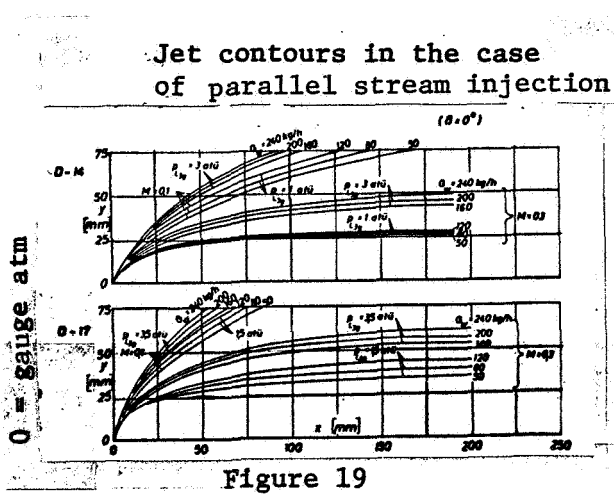

Figure 19

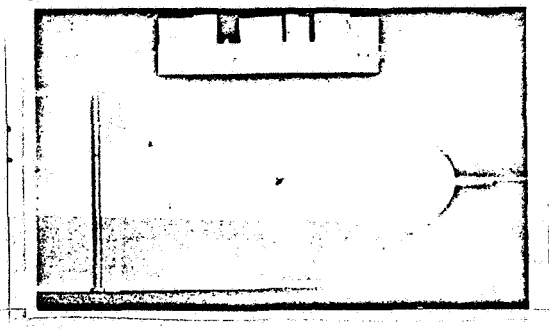

Figure 20

Attempts were then made to find a general expression for all jet contours and to derive the corresponding law and formula which would permit the advance determination of the jet contour to be expected from the given parameters. If the jet and attack angles are given, the jet contour is primarily determined by the velocities, impulses, and throughputs. Whereas it is possible to define clearly the velocity in the blower stream, the problem of establishing the effective jet velocity cannot be readily solved. In order to determine the values serving as radial penetration depth parameters, a number of vertical sections was drawn for various x values in Figure 19. By using these x values as parameters, the values of y, i.e., $y/\sin \alpha_{jet}$ were plotted on various abscissas. The first plot was against the fictive jet velocity $c_{fm} = I_{tot\ m} \cdot g/(G_A + G_W)$, and against the jet impulse or radial impulse. Since these plottings $I_{tot\ m}/G_A$. The curves thus obtained, however, still exhibited relatively strong scatterings. Only the plotting of $y/\sin \alpha_{jet}$ against $(G_A + G_W)$ gave satisfactory results (see Figure 21). The scatter here is no greater than the uncertainties of measuring the partly blurred jet contours. /36

The existence of curves against $(G_A + G_W)$ is a surprise at first sight. In order to explain this phenomenon, the acceleration phase of the droplets to almost the speed of air will be discussed qualitatively. In this discussion the droplets are considered being added to the air without an initial velocity. The air velocity decreases after exit from the nozzle approximately in accordance with the curves shown in Figure 22 along the path s.

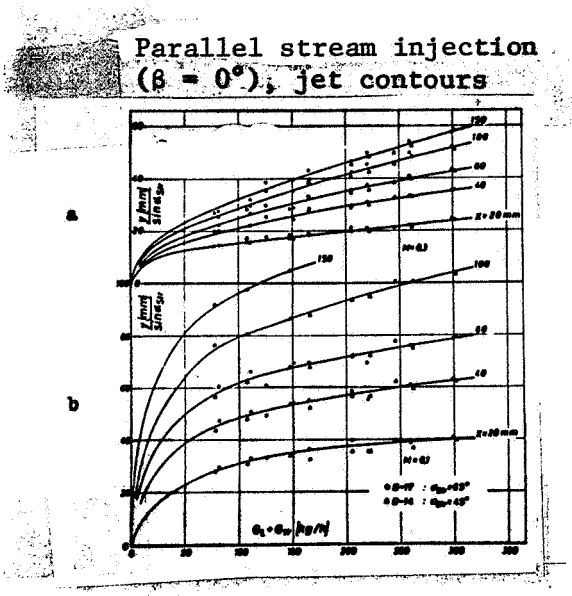

Figure 21

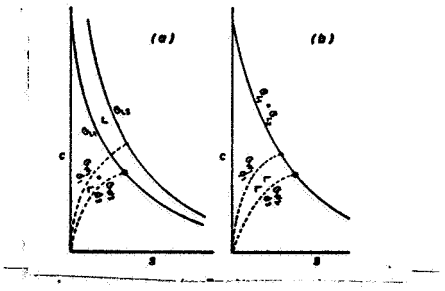

Figure 22
View of the acceleration phase

a) At G_W = const and G_A increasing, the atomizing air ratio $\lambda_{AN} = G_A/G_W$ will increase. The droplets become smaller (see Chapter 11.1). Owing to their smaller mass and to the higher air velocity, they will be accelerated more. Thus, they will attain the velocity of the air at approximately the same values of s as do the larger drops (see Figure 22a).

b) At G_A = const and G_W increasing, the atomizing air ratio will decrease. This is connected with an increase in the size of the droplets. Larger droplets require a larger acceleration path at the same air-muzzle velocity. Thus, the maximum velocity attained will be lower than in case of the smaller droplets (see Figure 22b). /37

In both cases (a and b), therefore, the smaller droplets have the higher maximum velocities upon attaining air velocity, and vice versa. It is likely that the droplet impulses will not differ to a significant extent. The experiments show that changes in G_A and G_W affect the contours in the jet range investigated to the same extent provided that M = const. If one considers the sum of the throughputs in terms of the product $G_A.(1 + G_W/G_A) = G_A.(1 + 1/\lambda_{AN})$, the factor G_A may be taken as the measure of the influence of the velocity, and the throughput ratio G_W/G_A i.e., the atomizing air ratio λ_{AN} as the measure of the influence of the droplet size on the penetration depths attainable.

In order to express the influence of the throughput on the radial penetration depth by means of an equation, the jet contours were plotted for a number of constant total throughputs $(G_A + G_W)$ against x in the case of M = 0.1 and M = 0.3 in Figure 23, on the basis of Figure 21. This figure shows that for a

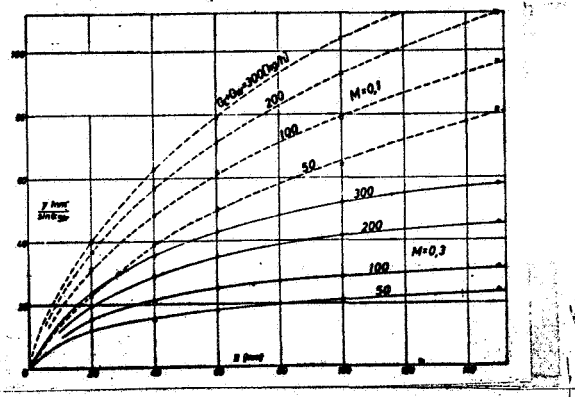

Figure 23. Parallel stream injection ($\beta = 0°$) jet contours

given value of x the percentage increase of the radial penetration depth becomes smaller in the transition from a low value $(G_A + G_W)$ to a higher, as does the Mach number. The expression $(G_A + G_W)^{0.9\sqrt{M}}$ was found to describe this relation. For the boundary condition where $M \to 0$, the value of this expression tends to approach unity; i.e., in this case the throughputs no longer affect the jet contour. Since deflecting perpendicular forces no longer prevail, the jet expands to its original angle (except for a certain small widening caused by turbulent mixing in the boundary zone) until it settles somewhere in the chamber. This distance of course depends on the operational point of the nozzle. The mist floating in the chamber cannot be pinned down in terms of measurement technique; in any event, it is of no interest insofar as practical application is concerned. If one correlates the factor $1/(G_A + G_W)^{0.9\cdot\sqrt{M}}$ with the ordinates $y/\sin\alpha_{jet}$, only one single contour curve is obtained for all Mach numbers (see Figure 24). By means of a further transformation,

$$\eta = \frac{y}{\sin\alpha_{jet}} \cdot \frac{M^2}{(G_A+G_W)^{0.9\cdot\sqrt{M}}} \qquad (42a)$$

$$\xi = x \cdot \sqrt{M} \qquad (42b)$$

/38

these curves practically coincide and form a general jet contour (see Figure 25, upper curve). The scatter is no greater than are the measuring uncertainties for the jet contours.

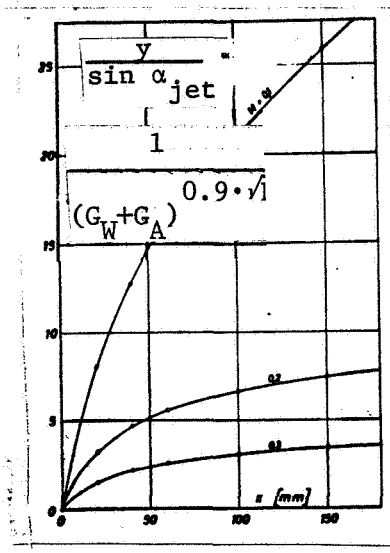

Figure 24. Jet contours with parallel stream injection (generalization).

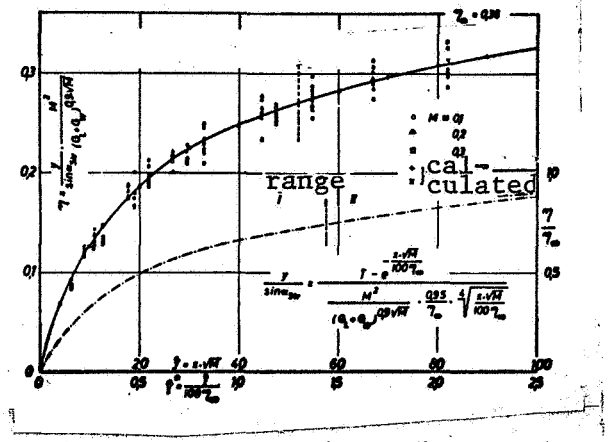

Figure 25. General jet contour with parallel stream injection ($\beta = 0°$), (cold, atmospheric ambient pressure).

Attempts were made to derive the equation for the general jet contour by using an e function:

$$\frac{\eta}{\eta_\infty} = k_1 \cdot (1 - e^{-k_2 \cdot \xi}) \qquad (43a)$$

The value of η_∞ was calculated as 0.36 from the diagram (Figure 25). This calculation using Equation (43a) was found to be correct only in the upper ξ range (II), however. A fourth root is superimposed in the lower range (I):

$$\frac{\eta}{\eta_\infty} = \frac{1 - e^{-\frac{\xi}{100\,\eta_\infty}}}{0.95 \cdot \sqrt[4]{\frac{\xi}{100\,\eta_\infty}}} = \frac{1 - e^{-\xi^{*}}}{0.95 \cdot \sqrt[4]{\xi^{*}}} \qquad (43b)$$

For the range boundary, we get $\xi^{*} = 4\,\eta_\infty$ hence $\xi = 400 \cdot \eta_\infty^2$ or $\xi = 0.52$. On the other side of the boundary (range II) the value of $\xi^{*} = 4\eta_\infty$ must be inserted under the fourth root in all cases, whereby the constant k_1 in Equation (43a) is obtained automatically. The solid curve in Figure 25 is the calculated curve. Under this curve, the quotient η/η_∞ against ξ^{*} was shown in a more general form (dot-dash line). Finally, the following expression is obtained by retransformation for the general jet contour: /39

$$\frac{y}{\sin\alpha_{jet}} = \frac{1 - e^{-\frac{x \cdot \sqrt{M}}{100\,\eta_\infty}}}{\frac{M^2}{(G_A + G_W)^{0,9 \cdot \sqrt{M}}} \cdot \frac{0,95}{\eta_\infty} \cdot \sqrt[4]{\frac{x \cdot \sqrt{M}}{100\,\eta_\infty}}} \qquad (44)$$

The dimensions to be inserted in this equation are: x and y in mm, G_A and G_W in kg/hr. The expression is valid for the approach flow of nozzle jets with cold air (T ≈ 300°K) at atmospheric ambient pressure. If the conditions are

different, appropriate corrections may be installed on the basis of subsequently performed hot tests and theoretical considerations (see Chapter 10).

7.2.3. Cross-stream injection

General laws will be derived for cross-stream [perpendicular] injection in a similar manner as for auxiliary injection, to obtain the jet contours in the investigated ranges. For this purpose, the available small-angle nozzles (D-16, D-15, D-13S, and D-12 with small mushroom) were fitted into one of the boundary walls in the anterior part of the measuring section in a vertical position, and extensive test series were conducted with various nozzle operation points and blow approach stream velocities. As an example, Figure 26 shows one of these tests (D-16, G_W = 160 kg/hr, p_{A3t} = 2.5 gauge atm, and M = 0.2).

After plotting all jet contours y against x, a reference value was again sought with the aid of which the contour points could be employed for the derivation of a law capable of being expressed with a formula. Since plotting against $(G_A + G_W)$ has been successful in the case of parallel injection, this was tried in the case of cross injection also. This type of plot however gave good curves for D-16 only. Eventually, the jet impulse related to air throughput emerged as a useable reference value. Although this was employed even in the case of parallel injection, it gave there higher degrees of scattering than did the reference value $(G_A + G_W)$. In the next picture, 28a, the penetration depths y are plotted against $100.I_{tot\ ax}/G_A$ for D-16 in case of two Mach numbers. Perfect curves were obtained for the other five nozzles investigated also. By replacing the air throughput in the reference value $100.I_{tot\ ax}/G_A$ according to the impulse expression $(G_A = g.I_{Aax}/c_{Aax})$, it may be considered to represent also the product of air velocity and relative impulse increase:

$$100.\frac{I_{tot\,ax}}{G_A} \sim c_{A_{ax}}.\frac{I_{tot_{ax}}}{I_{Aax}} \qquad (45) \qquad /40$$

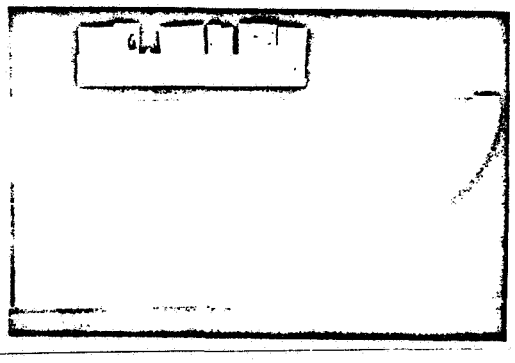

Figure 26

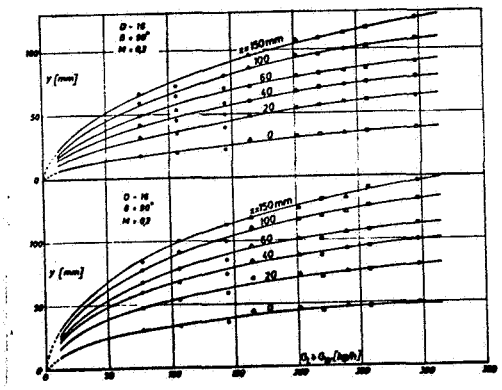

Figure 27

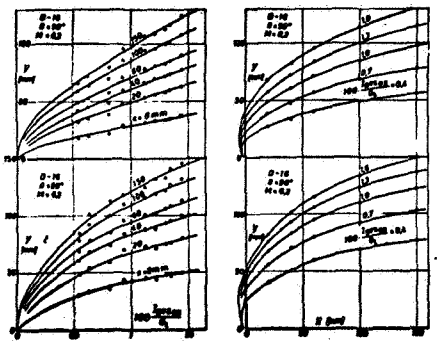

Figure 28

Thus, the jet contours y against x can be rendered only with the aid of the reference values introduced as parameters (see Figure 28b). We are dealing here with the external jet contour. It was not possible to find a method of rendering the internal jet contour although extensive considerations and experimental plottings were made. For the lower contour it may be said that it lies in most cases shortly behind the nozzle near the channel wall and detaches itself only in cases of high nozzle exit impulses and small approach stream Mach numbers.

The relation between penetration depth and the representative value of $100.I_{tot\ ax}/G_A$ was now characterized by a power formula. By means of an intermediate logarithmic plotting the exponent was established as 2/3, so that the value of the penetration depth y becomes $y = \text{const}\ (100 \cdot I_{tot\ ax}/G_A)^{2/3}$ if $x = \text{const}$ (see Figure 29a,b). By relating the value $(100 \cdot I_{tot\ ax}/G_A)^{2/3}$ to the ordinate, a plot against x yields only a single curve for any Mach number (see Figure 29c). Finally, it becomes possible to eliminate the influence of the Mach number by the following transformation:

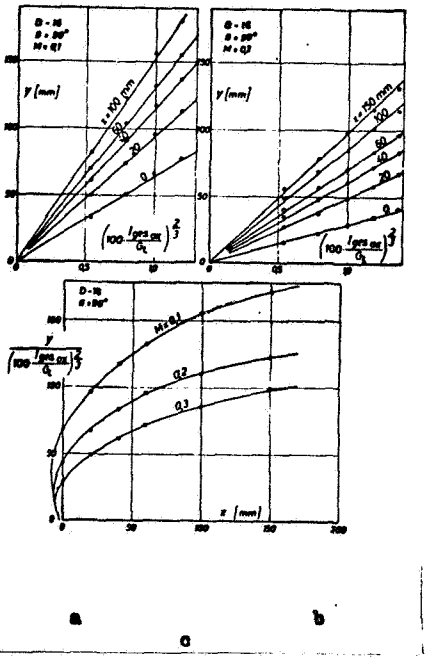

Figure 29

$$\xi = x \cdot \sqrt{M} \qquad (46a)$$

$$\eta = y \cdot \left(\frac{M}{100.I_{tot\ ax}/G_A}\right)^{2/3} \qquad (46b)$$

/41

In Figure 30 (lower curve), the general jet contour for cross-stream injection ($\beta = 90°$) is rendered as $\eta = f(\xi)$. Whereas nozzles D-16, D-15, and D-12 fitted well within the scattering range, nozzle D-13S fell initially too low, especially at higher Mach numbers (0.2 and 0.3). Since D-13S differs from the rest of the nozzles because of a very heavy torque, it is obvious that the jet becomes softer due to the twist, and this results in lower penetration depth, especially at higher approach-stream Mach numbers. Another correction factor must be introduced to cover this phenomenon. By means of the modified η transformation good correlation with

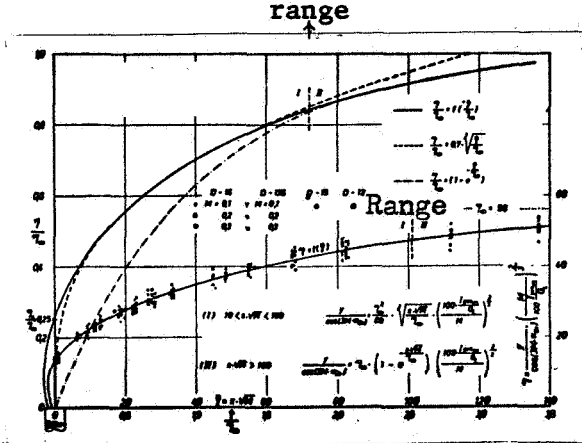

Figure 30. General jet contour reverse-flow injection ($\beta = 90°$) (cold, atmospheric ambient pressure)

the other nozzles was obtained for D-13S also. The mean measuring curve from this plotting was now again represented in the form of η/η_∞ against ξ/η_∞ as was done in case of parallel injection (upper solid line, Figure 30), whereby $\eta_\infty \approx 56$ was taken as the estimated boundary value for $\xi \to \infty$. In order to characterize the general jet contour by a formula, we set up another e expression:

$$\frac{\eta}{\eta_\infty} = (1 - e^{-\frac{\xi}{\eta_\infty}}) \tag{47a}$$

(dot-dash line in Figure 30). This expression nicely represents the contour in the upper range II ($\xi > 100$, i.e., $\xi/\eta_\infty > 1.8$). In the lower range I the jet contour may be approximated by a cubic root, except for the zone immediately around zero. For $-0.1 < \xi/\eta_\infty < +0.1$ the following equation applies: /42

$$\frac{\eta}{\eta_\infty} = \frac{\eta_\infty}{80} \cdot \sqrt[3]{\frac{\xi}{\eta_\infty}} \tag{47b}$$

(dashed line curve in Figure 30). The intersection point of the general jet contour with the extended nozzle axis lies at $\eta_o = 0.25 \cdot \eta_\infty$. Retransformation gives the following expressions:

$$\text{(I)} \quad \frac{y}{\cos(3M \cdot \alpha_{Tq})} = \frac{\eta_\infty^2}{80} \cdot \sqrt[3]{\frac{x \cdot \sqrt{M}}{\eta_\infty}} \cdot \left(\frac{100 \cdot I_{tot\,ax}/\sigma_A}{M}\right)^{2/3} \tag{48a}$$

$$\text{(II)} \quad \frac{y}{\cos(3M \cdot \alpha_{Tq})} = \eta_\infty \cdot (1 - e^{-\frac{x \cdot \sqrt{M}}{\eta_\infty}}) \cdot \left(\frac{100 \cdot I_{tot\,ax}/\sigma_A}{M}\right)^{2/3} \tag{48b}$$

With the aid of these expressions it is possible to determine in advance the jet contours to be expected in case of cross-stream injection if the nozzle parameters and approach stream Mach numbers are known. The accuracy here, too, is on the order of magnitude of the maximum attainable measuring accuracy for the jet contour (approximately 10%). The validity of the formula extends to the

range investigated in this project for the individual parameters and to the ambient conditions employed here (cold approach stream at atmospheric ambient pressure).

7.2.4. Reverse Flow Injection

In these investigations the nozzles were fitted centrally in the test section and the jets were photographed for various operational and approach stream conditions. The small-angle nozzles (D-16, D-15, and D-13S) were used here too because the wide-angle nozzles are not suitable for this purpose, as will be explained later.

Figure 31 shows a portion of the reverse-flow injections performed (nozzle D-15). The next picture, Figure 32, is the jet photograph of a nozzle operating point (D-16, G_W = 200 kg/hr, p_{A3t} = 2.5 gauge atm, and M = 0.2). The approximately parabolic jet contours in this injection mode are very difficult to draw since, due to the opposing velocities of the approach stream and the nozzle jet, strong turbulence is evident which distributes the jet throughout the entire measuring section after a very short run. Thus, no more detailed consideration will be given to this most uncertain contour. Emphasis will be given to the axial penetration depth x, defined as the distance between the nozzle mouth and the jet inversion point. The axial total impulse $I_{tot\ ax}$ was found to be a representative value for the axial penetration depth. Owing to the small jet angle ($2\alpha_{jet} \approx 15°$ to 18°), the approximation $I_{tot\ ax} = I_{tot\ m} \cdot \cos \alpha_{jet} \approx \approx I_{tot\ m}$ was again employed; this is permissible because of the limitations of measuring accuracy. The Mach number dependence may be expressed by $M^{1.5}$. In the plotting of x against $I_{tot\ ax}/M^{1.5}$, a practically identical set of curves is obtained for D-15 and D-16, differing merely a little in the lowermost region (see upper curve in Figure 33). Good correlation is evident in the

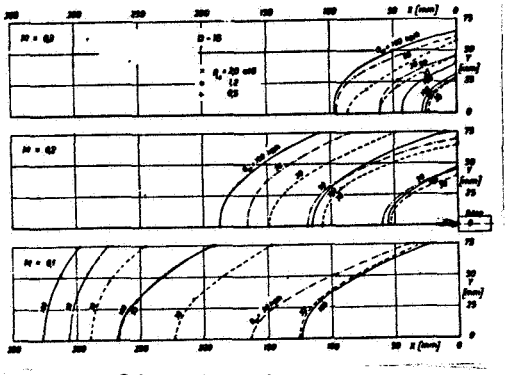

Figure 31. Axial penetration depth reverse-flow injection

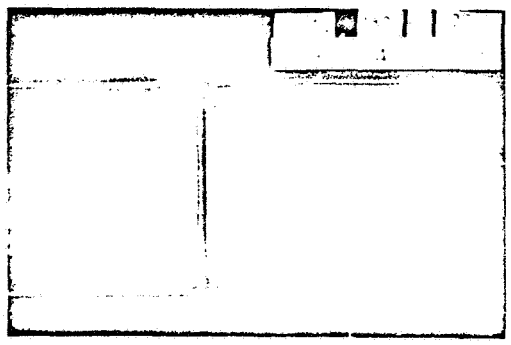

Figure 32

medium and upper regions. It should be noted, however, that at high penetration depths the measuring uncertainties for the blurred jet are great and this gives us a greater scatter in the graph. The curve corresponding to nozzle D-13S is considerably lower. As in the case in cross-stream injection, the

jet-softening effect of the torque manifests itself here in the jet. This effect is much greater in the present case: it can be expressed by the term $\cos^5\alpha_{Tq}$. By taking in Figure 33 the value of $x/\cos^5\alpha_{Tq}$ as the ordinate, the curve for nozzle D-13S will also coincide with those for the others (D-15 and D-16), these nozzles being considerably torque compensated as triple flow nozzles. A linear approximation provides a good approximation for the slightly curved line: /44

$$\frac{x}{\cos^5\alpha_{Tq}} \approx (20 \div 22) \cdot \frac{I_{tot\,ax}}{M^{1,5}} \qquad (49)$$

The dimensions to be inserted are: x in mm and $I_{tot\ ax}$ in kg.

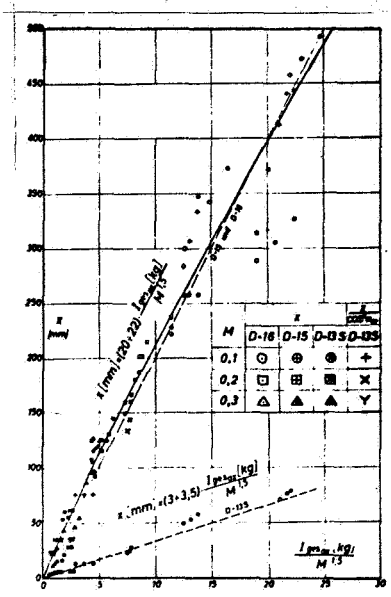

Figure 33. Penetration depth with reverse flow injection (β = 180°)

In order to investigate the effect of the jet angle on the axial penetration depth, nozzle D-12 (α_{jet} variable) was also briefly studied in reverse-flow mounting. This study showed that the wide-angle jets have only very slight axial penetration depths at high and average approach stream Mach numbers (an effect similar to that of the torque angle). The radial penetration depths, however, are throughout higher than in parallel stream injection at the corresponding operating points.

At low Mach numbers, small amounts of water, and large amounts of air, the jet exhibited a remarkable degree of unsteadiness, characterized by a sudden reversal to high axial penetration depth (hereafter designated as 'long jet'). A closer investigation led to the following interpretation of this phenomenon: Small water and large air throughputs result in relatively small jet angles for D-12 (see Figure 15), at the same time we get high axial velocity components. These conditions prevent the penetration of the injected air into the jet cone (see sketch in the top part of Figure 34); it flows along the jet contour in a direction opposite to that of the jet motion. This results in the already mentioned turbulence, which exists to a considerable degree throughout the entire test sections cross section, together with a good degree of liquid distribution. In the case of the 'short jet', usually occurring in D-12 (see sketch in the bottom part of Figure 34), the injected air enters the jet cone, turns around, and flows in the same direction as the jet contour, which in this case will remain relatively sharp owing to a lesser degree of turbulence.

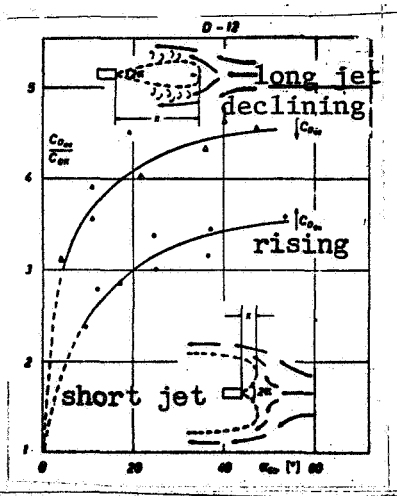

Figure 34. Jet reversal in reverse-flow injection.

Jet reversal can be best expressed by plotting the ratio of jet velocity, c_{Nax} and injection velocity, c_{CC}, as a function of the half jet angle, α_{jet}. The reversal point occurs at various points depending on the /45 degree of decreasing or increasing jet velocity. These investigations showed that for all practical purposes only small-angle nozzles are suitable for reverse flow injection.

8. Flameholder and Nozzle Jet (Low Temperature Experiments)

8.1. Summarizing Evaluation of the Various Principal Combustion Chamber Flameholders

To make an advance selection of suitable flameholders for the application of the present fuel system in principal combustion chambers, the principal combustion chamber was dismounted from the intake casing and replaced with plexiglass tubes. As a result it was possible to observe the diffusion of the nozzle jets in the (cold) combustion zone. The term flameholder is here applied to built-in components at the mouth of the flame pipe which generate turbulence or the frontal manifolding of the fire tube. Although the present low temperature experiments do not exactly duplicate the conditions existing in a heated combustion chamber, the tendencies and evaluations concerning the flameholders during the low temperature experiments do not vary in the subsequent thermal experiments. Flameholder experiments are described in detail in DFG research report Tr 13/18. The present work represents merely a short summary. In Chapter 12.2. we will discuss in more detail several essential points in the course of the explanation of the experimental chamber design.

F-1, perforated flameholder: The primary air here is injected through perforations in a plane disc or a conical foundation into the nozzle jet. If the arrangements and the size of the holes are unpractical, pulsations can easily be induced. A correct arrangement results in good radial penetration depths after these flameholders, especially in the case of the perforated cone.

In the latter case, the radial penetration depths of the nozzle jet must be stopped up with an accelerated counter-air current [air streak]. In the case where the jet was permitted to precipitate next to the fire tube, combustion turned out to be poorer. The perforated flameholder of the F-1 type yields good microturbulences. The ignition limits, however, existed relatively close to each other because of the absence of a clearly defined recirculation zone (macroturbulence). Extensive losses of pressure can also be named as a disadvantage.

F-2, ring slot flameholders: It was found possible to eliminate pulsation tendency of the F-1 type by concentrically arranging a number of ring slots on a plane or conical foundation. The nozzle jet, however, was compressed by the /46
oncoming primary air to such an extent that only insufficient radial penetration depths could be obtained. For this reason, flameholders of type F-2 are impractical; in addition, they result in considerable pressure losses.

F-3, torque flameholders: In order to prevent the primary air from acting in the ring slot model directly upon the nozzle jet and diminishing the penetration depth, the slots were expanded and provided with small scoops. These serve to decrease the axial velocity of the primary air and give rise to tangential components. The direction of the tangential components alternates in opposite directions from one slot to the next slot. As a result, high relative velocities together with good turbulence are generated in the transition zones. A combination of the strong microturbulence and the reduced axial velocity produces satisfactory penetration depths. It was found expedient to cover the inside wall of the fire pipe with an accelerated counter-air current. The flameholder F-3 also exhibited narrow ignition limits in the hot experiments because the recirculation zone in the center of the fire pipe was not completely formed. Smaller losses in pressure, however, were recorded with this flameholder. The absence of a localized turbulence caused the flame to become unsteady. Generally, however, type F-3 can be considered as quite serviceable.

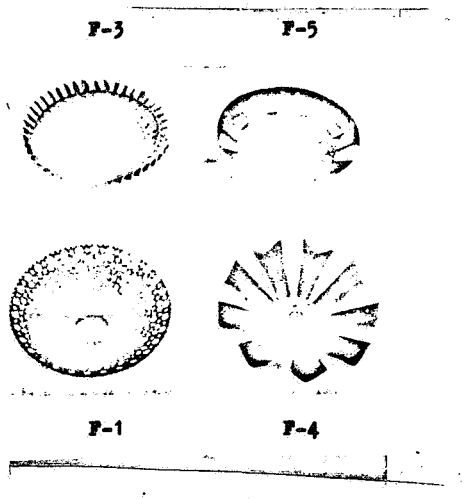

Figure 35

F-4, radial burners. In this type of flameholder it was found that the penetrations of the jet behind the obliquely radial angle ribs extended to the wall of the fire tube. The nozzle jet between the radial ribs attained, in fact, only half of the flame tube radius. As a result, the irregularity of distribution increased with increasing radius in the peripheral direction. The radial burners are nevertheless classified with the serviceable flameholders in this fuel system.

F-5, torque-radial burners: The frontal side of these flameholders is divided into three annular zones with sheet metal rings. The two on the inside were armed with small countertorque scoops, whereas the radial ribs [fins]

served to ensure adequate recirculation and consequently a wide operational range. These flameholders gave the best results in the thermal experiments. Figure 35 pictures the flameholders F-1, F-3, F-4, and F-5. /47

8.2. Afterburning-Chamber Flameholder in Nozzle Jet

8.2.1. Parallel air injection

A number of angle profiles of various magnitudes and arrangements were placed in the nozzle jet in order to investigate the influence of various afterburning chamber-flameholders on nozzle jets. At first the nozzle was attached parallel to the direction of the parallel air flow. The introduction of angle profile flameholders into the nozzle jet generally results in an expansion of the jet. This phenomenon is illustrated in Figure 36 by means of several examples for D-12. The variation in the contour of the jet caused by the flameholder can be expressed in the following manner:

The expansion of the jet has its origin about 2.5 to 2.8 $\cdot b$ in front of the flameholder (b = width of the flameholder). If the distance between flameholder and nozzle is $\ell_S > 2.7 \cdot b$, then the contour of the jet will remain unchanged during the first section of the jet path. If the distance is $\ell_S < 2.7 \cdot b$, then the jet begins to expand even at the mouth of the nozzle. A jet expansion of approximately b/2 is already present in the plane of the flameholder. The expansion reaches a magnitude of b at a distance 2.7 $\cdot b$ after the flameholder and now becomes superimposed without any noticeable change on the jet contour without flameholder. The course of Δy in the range between 2.7 $\cdot b$ in front of and 2.7 $\cdot b$ behind the flameholder corresponds approximately to a sine curve. In Figure 37, this course is plotted in the form of $\frac{\Delta y}{b/2}$ against $\frac{\bar{x}}{b} = \frac{x-\ell_S}{b}$. The transformation of the abscissa $x^{*}[^{\circ}] = \bar{x}/0.03b$ makes it possible to express the principle as follows: /48

$$\frac{\Delta y}{b/2} = \frac{1}{2} \cdot (1 + \sin x^{*}) = \frac{1}{2} \cdot (1 + \sin \frac{x - \ell_S}{0,03.b}) \qquad (50)$$

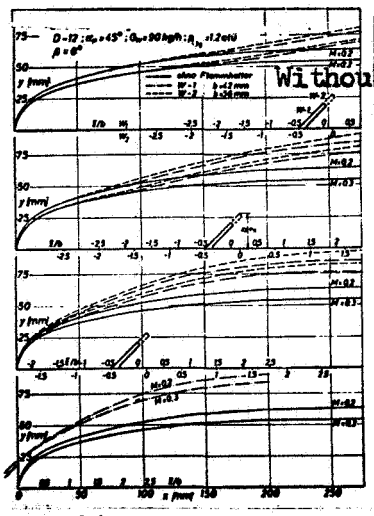

Figure 36. Jet expansion with flameholder
D-12; α_M=45°; G_W=90 kg/hr; A_{3_t}=1.2
gauge atm s = 0°

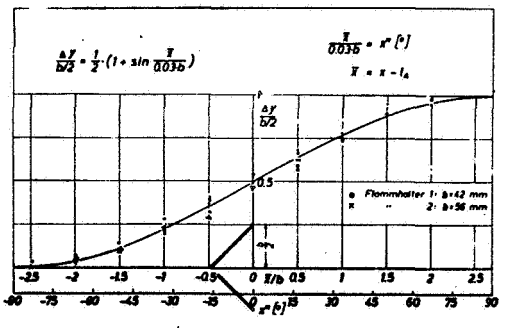

Figure 37. Jet expansion with flameholder

As indicated by the following illustration (Figure 38), the flameholder effects a change in the local liquid concentration over the cross section of the test section, especially in an area up to 3b after the flameholder. In addition there is a reflux of liquid of the turn around point of the recirculation zone which is approximately 5 to 6b away. Only very little liquid reaches the area behind the flameholder upon the injection of water into cold air, because the droplets fly past (are ejected from) the low-pressure zone as a result of their inertia. For this reason the fuel must be substantially evaporated upon arriving at the flameholder, because otherwise it would not reach the recirculation zone and would not obtain any adequate retention times. Figure 38 indicates that an increased concentration is present directly in front of the flameholder and in the extension of the flameholder side. A relatively uniform distribution does not occur until behind the turbulent zone (see Chapter 9.2, distribution measurements).

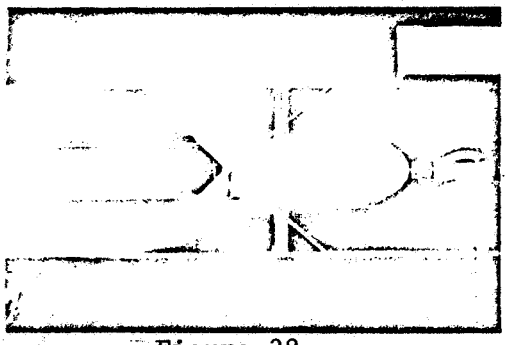

Figure 38

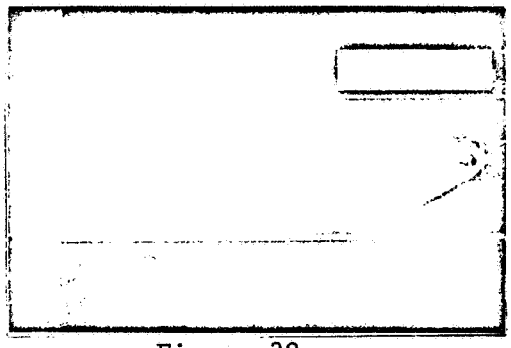

Figure 39

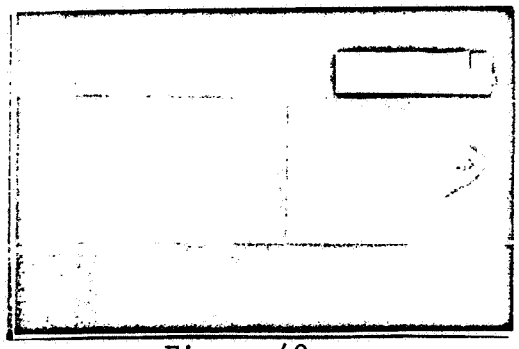

Figure 40

If the nozzle is located directly in the flameholder (see Figure 36, bottom, /49 and Figure 39), then the jet is forced on when x = 0 and proceeds practically at the angle of the flameholder. Obviously, the contours in the forward region are influenced mainly by the flameholder and less by the nozzle heading. The jet is blasted over the imaginary extensions of the flameholder sides, which normally envelop the jet (see Figure 40), only in the case of low approach current Mach numbers and high radial momenta. The liquid distribution over the test sections cross-section is very good, as can be seen from Figures 39 and 40. It must be expected, however, that the direct injection into the turbulent zone during the hot experiment causes a considerable quantity of the fuel to evaporate in that place, whereby the temperature of the vortex core, which is a determining factor for the combustion stability and the ignition boundaries, drops considerably. Later thermal experiments with this arrangement resulted in merely a slight operational range and a pronouncedly yellow recirculation zone with soot precipitation.

In the case of a staggered flameholder arrangement (two planes of flameholder, see Figures 41 and 42), the contours can no longer be pursued after the second flameholder plane; merely the above mentioned outflow along the sides

of the flameholder is noticeable. The changes in contour are the same as those for the first flameholder, as described above.

The interval between the two flameholder planes as well as the distance of the flameholders in the second plane have a pronounced influence on the total flow image. The variation of these intervals gave rise to a very noticeable optimization in the measurements, for which there exist the most uniform distributions after the second flameholder plane. This optimization is practically independent of the Mach number of the approach current and nozzle operating point. It reads as follows: The second flameholder plane is most expediently located closely behind the inversion point of the first flameholder (distance approximately 6b). The optimum distance from center to center of the flameholders in the second plane is 3b. If the injection occurs before the first flameholder, then the distance between this and the nozzle (ℓ_S) is at first recorded at 4b (optimum in view of the distribution behind the flameholders). The exact determination of the necessary separating interval ℓ_S does not depend on the width of the flameholder. The principal factors (for a given fuel) are temperature and velocity at the entrance of the afterburning chamber. Investigations related to this are not discussed until later (see Chapter 16.2.2.). /50

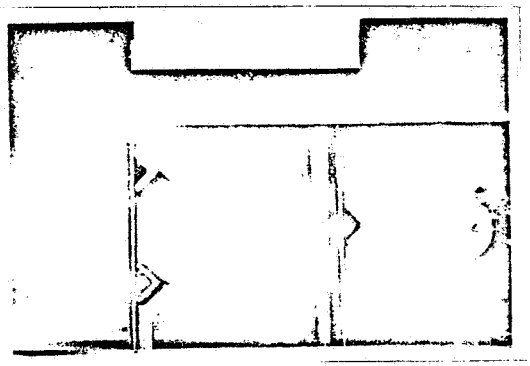

Figure 41

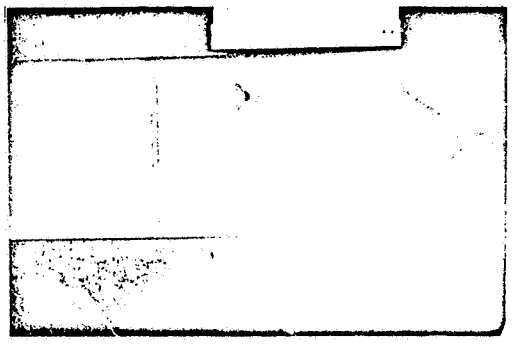

Figure 42

8.2.2. Cross-stream Injection

In cross-stream injection, the angular flameholders were placed in a position lateral to the nozzle jet (see Figure 43a) or parallel to the direction of the jet (see Figure 43b), where the nozzle in each case was caused to inject in front of (position 1) and behind (position 2) the flameholder. Only one of these four arrangements proved to be possibly useful (b1). In that particular arrangement (a), a very strong dependence on nozzle heading and the Mach number of the approach current became evident. A uniform image behind the flameholder appeared only in the case of great nozzle momenta and small approach current Mach numbers, whereas in all other cases the principal part of the jet was forced toward the wall of the test section on the side of the nozzle (especially in arrangement a1). As a result, the penetration depths were reduced considerably and the distributions after the flameholder became greatly asymmetrical. Arrangement (b2)

proved somewhat more favorable due to the position of the nozzle in the pressure zone of the flameholder. The penetration depths corresponded approximately to those without flameholder.

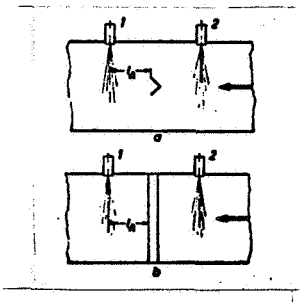

Figure 43. Reactive current injection

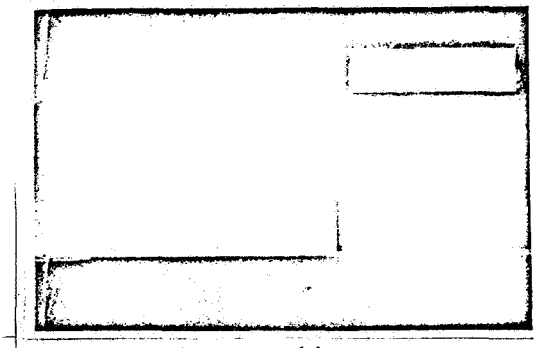

Figure 44

A very substantial increase in penetration depths was achieved with arrangement (b1) (nozzle jet is located parallel behind the flameholder). A part of the jet collided with the opposite wall of the test section in the case of all headings. A more or less substantial portion, however, was already picked up by the vorteces of the flameholders and distributed extensively over the cross section (see Figure 44). For the achievement of favorable results, the distance ℓ_S between the nozzle and the flameholder was very important. If ℓ_S was very large, the jet was no longer picked up by the vorteces; if they were very small, a substantial part of the jet was pressed against the flameholder and was discharged there. The optimum value can be defined as follows: The most favorable distance between nozzle and flameholder exists when as large as possible a portion of the jet is picked up by the vorteces, when the distributions are as uniform as possible, and when as little fluid as possible collides with the flameholder. The change point was determined with variations of ℓ_S. The optimum distance was found to be $\ell_S/b \approx 2.5$ to 3. The relationship is only little influenced by nozzle momentum, Mach number, size of the flameholder, and jet angle. The smaller values (approximately 2.5) are a result of great nozzle momenta, jet angles, and angle profiles as well as of small Mach numbers. The optimum value ℓ_S/b for opposite parameter magnitudes is in the proximity of 3.

/51

Even though an afterburning chamber with a diameter more than one meter must be charged through outside nozzles in the case of arrangement (b1) because of the large penetration depths, the practical significance even here, as in the case of the auxiliary jet injection behind the flameholder, does not seem to be very great (decrease of the temperature of the vortex core, see p. 42).

8.2.3. Reverse-flow Injection

The nozzle in afterburning chambers with direct reverse-flow injection is under certain circumstances subjected to intense thermal influences; therefore, the reverse-flow injection was modified somewhat. Subsequent thermal

experiments, however, indicated that even direct reverse-flow injection is feasible and yields excellent results (see Chapter 16.4.). In this modified reverse flow injection the nozzle was again attached to the wall of the test section and was directed diagonally to the jet (angle of injection β = 135 to 150°). Thus, we are dealing with a combination of direct reverse flow injection with cross-stream injection.

Two arrangements which are represented in Figure 45, were investigated. Arrangement (a) indicates great sensitivity due to changes of headings and Mach numbers, just as was the case with the corresponding cross-stream arrangements. Figure 46 reproduces several experimental results. An increasing Mach number causes a decrease in the influence of the Mach numbers and the /52
headings. Good conditions after the flameholder develop only with certain correlations of heading, Mach number, and distances a;c in the lower region. Changes in heading or Mach number without simultaneous adjustment of the distances a and c lead to a rupture or puncture of the nozzle jet. The larger flameholder (top, Figure 46) is less sensitive to changes in the Mach number due to the more intense return flow zone. The optimum curves here are somewhat flatter and are at a slightly higher level than those of the smaller flameholder. The supersensitivity exhibited would render the practical application of this arrangement highly questionable. Figure 47 represents one of the few favorable headings.

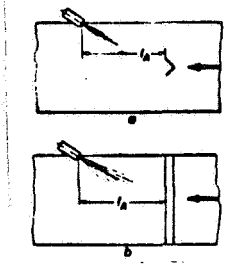

Figure 45. Diagonal-reactive current arrangement

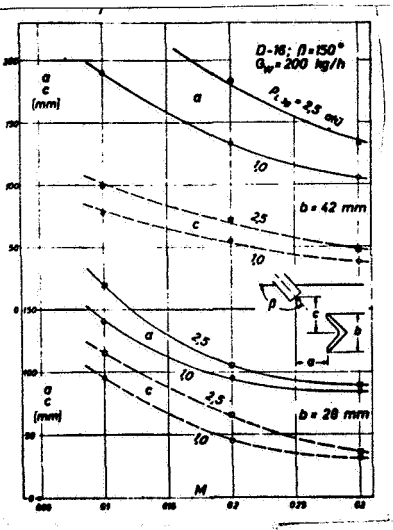

Figure 46. Optimum intervals

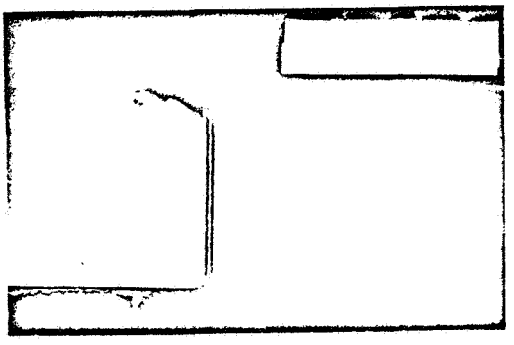

Figure 47

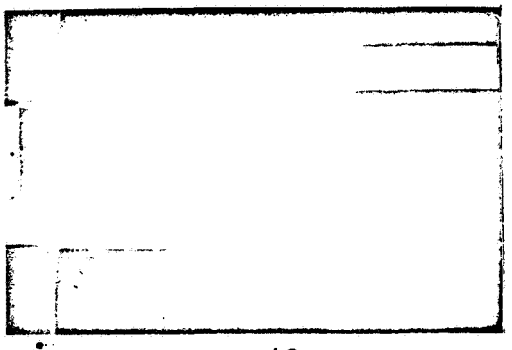

Figure 48

The arrangement according to Figure 45b, on the other hand, looks much more feasible (jet and flameholder on one level), in which the nozzle jet is quasi-screened from the flameholder. Penetration depths, similar in magnitude /53
to those of the corresponding cross-stream arrangement, are realizable in this way. The experiments conducted yielded the law $\ell_S \approx x + 4b$ for the optimum distance ℓ_S, where x represents the reverse-flow penetration depth without flameholder as determined in Chapter 7.2.4. The flameholder thus will have to be oriented in such a way that the change point of the jet will be located within the return flow zone of the flameholder (≈5 to 6b). This condition gives promise of a wider field of application than the arrangement presented in Figure 45a, because the air flow accelerated in the flameholder does not force the jet from the flameholder and thus does not cause an interruption. It becomes evident that the angle of injection β in a certain region (≈ 135 to 150°) has hardly any influence on the optimum value of ℓ_S. By means of β, on the other hand, it becomes possible to vary the radial penetration depth and to influence the distribution. The most expedient results were obtained when the nozzle was installed with intervals of ℓ_S in such a way that the center line of the jet passed through the point of intersection of flameholder and axis of test section (see Figure 48).

The serviceability of the present arrangement can also be estimated already in the thermal experiment; it represents an arrangement seemingly parallel to that of the vaporizing combustion chambers. In the latter the fuel is injected in the direction parallel to the parallel current and conducted into the vaporizing tube with a small amount of air. As soon as the mixture in the pipes has passed through the hot combustion zone, the vapor is insufflated parallel to the direction of the reverse flow. In the arrangement on Figure 45b described here, the jet which already contains air flows through the hot combustion zone without piping. Prior to reaching the flameholder vorteces the jet probably becomes very hot and evaporates. The temperature of the vortex core decreases only slightly, thereby seeming to assure good combustion. The quick separation of the jet in as favorable an environment as possible can eventually lead to a value below that of ℓ_S mentioned above (the formula determines a maximum value). As a result, a wider area of operation is made possible. The arrangement investigated here furthermore yields shorter construction dimensions for the chamber, because the separation length ℓ_S overlaps with the combustion length ℓ_C, whereas both lengths are arranged consecutively in the case of auxiliary current injection. Chapter 16.3. discusses the extent to which these conceptions are confirmed experimentally.

9. Distribution Measurements

9.1. Without Flameholder

The spatial distribution of the fuel in the combustion zone has a con- /54
siderable influence on the quality of the combustion and the distribution of the temperature in the combustion chamber. The distribution curves must

be taken into consideration when selecting the appropriate nozzles and do not only provide important clues to the formation and length of the necessary propagation zones but also answer the question concerning the structure and position of the flameholder.

In order to investigate the problem of fuel distribution in the combustion chamber, distribution measurements were conducted in the jets with a comb probe for intercepting flow in the case of D-12 with various nozzle headings, velocities of blower jet, and directions of blower jet. The following illustration 49 represents a small selection of the curves plotted, which make a number of statements possible. The ratio of intercepting height h (mm) to testing time t (min) was chosen as the ordinate.

A typical M-shaped distribution (see Figure 49a,b) for turbulence nozzles appears with parallel current injection ($\beta = 0°$). The concomitant asymmetry can probably be explained by inaccuracies in the manufacture of the nozzle mouth or by the misorientation of the nozzle in the test section. This latter conjecture is supported by the fact that a shift takes place alternately to the left and to the right. The distribution curves are influenced by the velocity of the approach flow in all nozzle headings to such a great extent that, with constant nozzle heading at diminishing Mach number of the approach flow, the M-shape becomes flatter and wider. A G_W change of the nozzle causes a synonymous change in height and width of the distribution curve due to the associated change in the jet angle (increasing with G_W). If the velocity of the approach flow (the propulsion unit throughput for partial load) decreases simultaneously with diminishing G_W, then the influence tendencies on the distribution run in the opposite direction. The distribution curves in that case do not undergo a noticeable change. Figure 50 represents a photograph of the collecting battery for one of these measurements ($\beta = 0°$, $G_W = 180$ kg/hr, $p_{A3t} = 2$ gauge atm, $M = 0.2$).

The distribution curves for cross-stream injection ($\beta = 90°$) show a distinct point (see Figure 49c). The point moves to the outside (away from the nozzle) with decreasing approach flow Mach number, and the height of the point becomes smaller. At the same time, the base of the distribution curve (the width of the jet) becomes larger with decreasing approach flow Mach number. Even though the nozzle D-12 was provided with a small mushroom angle $\alpha_M = 15°$ in these experiments for the realization of small jet angles (high axial exit momenta), the penetration depths in the direction of the jet exit are not satisfactory in the case of average and high approach flow Mach numbers. A distinct narrow-jet nozzle yields better results in each case of cross-stream injection, as has already been shown in the jet investigations with D-15 and D-16. /55

In the case of reverse-flow injection ($\beta = 180°$) the distribution curves (see Figure 49d) confirm what has already been indicated by the jet contours illustrated in 7.2.4.: The liquid distribution over the test section is much more uniform for all approach flow Mach numbers than for parallel current injection and, moreover, is not as dependent on the Mach numbers.

The M configuration of the curves is no longer recognizable. The maximum is now found in the center of the chamber, from which point the curves decrease at first slightly and then steeply toward the edge (left half of the figure). The irregularities in the right side of the figure are due to the supply lines of the nozzle.

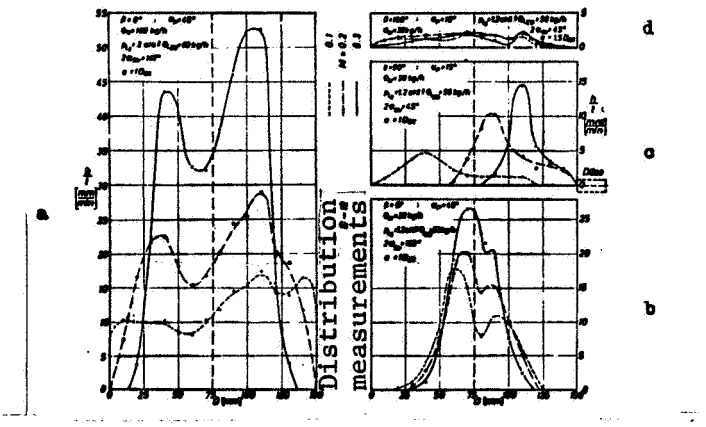

Figure 49

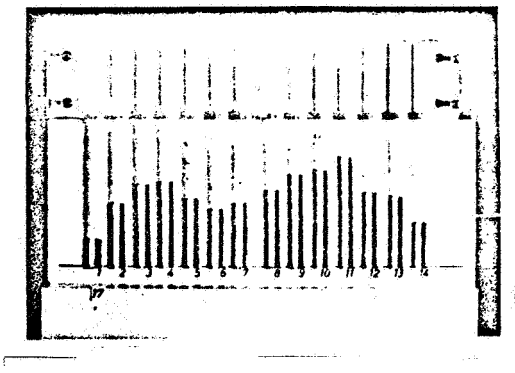

Figure 50

9.2 With Flameholder

The distribution of the liquid over the cross section of the test section is recognizable, at least approximately, even in the existing photographs of the jet. The distribution curves recorded by means of the comb probe do not indicate anything to the contrary. In the case of parallel current injection in front of the flameholder, the downward slope of M-shaped distribution curves without flameholder becomes deeper. The concentration in the center immediately after the flameholder is equal to zero, whereas high peaks are /56
formed in the exit direction of the angle sides. The curves flatten out with an increase in the distance from the flameholder, until they exhibit hardly any waves at a distance > 10b. With equal nozzle headings the concentrations measured are higher for M = 0.3 than for M = 0.2, because the cross section of the jet is smaller. For the same reason the present concentrations decrease with larger flameholders (larger b). If the nozzle is located directly in the flameholder, then the distribution curve expands in comparison to the jet without flameholder over the cross section corresponding to the expansion of the jet. The concentrations in the center are higher at the 10b distance than in the case of injection in front of the flameholder, that is the perturbations due to the flameholder are compensated sooner.

In the case of reactive current injection after the flameholders the distribution curves exhibit sharp peaks at the opposite wall of the test section, especially with low approach flow Mach numbers and high nozzle exit momenta. The peaks are only little compensated with increasing distance from the flameholder. When the cross-stream was injected diagonally behind the flameholder

in the associate plane, the resulting distributions were found to be the most uniform.

Although a number of error possibilities prohibit the results of these distribution measurements from being viewed in a strictly quantitative sense, the tendencies sketched above are important purely qualitatively for the design of the chamber.

10. Investigations of Contour under Changed Conditions

10.1. Atomization of Fuel in Cold Air

If fuel is now atomized instead of water (low-temperature experiments), then the size of the droplets will decrease for uniform relative velocities (that is, practically uniform air throughputs). This becomes evident even in Equation (4), because the surface stresses σ of water and kerosene will be approximately 3:1 (water 74 dyn/cm, kerosene 24 dyn/cm at 20°C). The quantity of the droplets increases as a function of the diminishing droplet size for uniform liquid throughput ($G_W = G_F$). Thus there exist two opposite influences on the penetration depth: first, the smaller droplets lose their energy sooner, which would decrease their ability to penetrate deeply, and second, the increased quantity of droplets strengthens the effect which, in comparison to the penetration depth of a single drop, increases the penetration depth of a jet (see p. 13 and 36 to 37). In addition, Abramowitsch maintains that the jet exiting from the nozzle has principally the effects of an air jet in which type and magnitude of the impurities are of secondary importance next to momentum, air throughput, and throughput ratio (G_{liquid}/G_{air}). The penetration depths, however, were correlated with these values. Consequently, no extensive changes in the penetration depths of the jet should be expected despite the changes in the atomization characteristics. /57

In order to clarify this question, several atomization experiments were conducted with fuel in cold air current. It became evident in the process that for appropriate nozzle headings (throughputs) the contours of the jets in the two cases can hardly be distinguished from one another. The contours recorded with kerosene were in each case located between the average value curve and the lower dispersion limit of the general contour representations (Figures 25 and 30). In plotting y_{fuel} against y_{water} a straight line was obtained with the slope ≈ 0.95. With this correction factor the contours of fuel jets can be determined from the contours of water jets with an adequate degree of accuracy.

10.2. Atomization of Water in Hot Gas

Prior to the atomization experiments in a hot gas jet, it was necessary to examine the outlet profiles of the heated chamber (intake profile of the test section). In the following Figure 51 the velocity profiles are sketched at the intake and outlet [exhaust] of the test section as well as the profile of the intake

temperature and of CO (the latter was recorded with URAS infrared gas analyzer). The chamber heading here was $M_5 = 0.3$ and $t_{5t} \approx 580°C$ or $T_{5t} \approx 850°K$, where the chamber was not extended fully. It was due to the effect of the temperature profile that the velocity profile of the hot chamber exhibits a slight increase in the center as compared with that of the cold chamber (Figure 18); this phenomenon must be taken into consideration with respect to the changes in contour discovered later on.

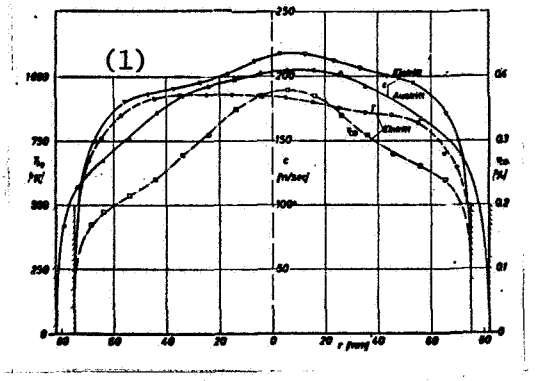

1. Profiles of the high-temperature experiment
2. Intake
3. Outlet
4. Intake

Figure 51

At this time an attempt will be made to make a rough estimate of the changes during atomization in hot gas. The actual process of atomization, which occurs directly at the nozzle, exhibits hardly any variation because the atomizing air is heated only slightly in the short section of the piping from the wall of the test section to the nozzle. The same is true of the liquid. For all practical purposes, therefore, the conditions existing at the source of the jet have remained unchanged in both cases (same droplet size during disintegration, same initial momenta and directions). The expansion of the jet, however, is now exposed to influences which differ from those of the low-temperature experiment. /58

If hot gas is blown against the nozzle jet, then the velocity is greater even if the corresponding Mach number remains the same. As a result of a smaller value in case of hot gas, the dynamic pressure of course decreases even though the velocity of the blower jet rises with $\sqrt{T_{st}}$ for the same Mach number. Furthermore, the diameter of the droplets decreases as a result of the evaporization. Thus, the Reynolds number over the diameter of the droplets becomes smaller for initially uniform jet velocity. The influence of viscosity must be added to this; it rises from $\nu_{A20°} = 1.5 \cdot 10^{-6}$ to $\nu_{A500°} = 100 \cdot 10^{-6} m^2/sec$. This strong decrease in the Reynolds number, according to Figure 1, results in a corresponding increase on the C_R value. The divergent and partly opposite influences overlap and probably serve to reduce the penetration depths in their final effect.

The extent of this decrease will now be determined experimentally. For this purpose a series of experiments was conducted with D-17 during injection of a parallel stream and with D-16 during reverse-flow injection. Figures 52 and 53 represents the comparison of low-temperature and thermal flow (chamber heading: $M_0 = 0.3$, $t_{5t} = 580°C$; nozzle heading: nozzle D-16, $G_W =$ 160 kg/hr, $p_{A3t} = 1.6$ gauge atm. These illustrations result in the following

conclusions: The contours remain unchanged in both cases for the first section of the passage subsequent to exiting from the nozzle (approx. 20 to 25 mm).

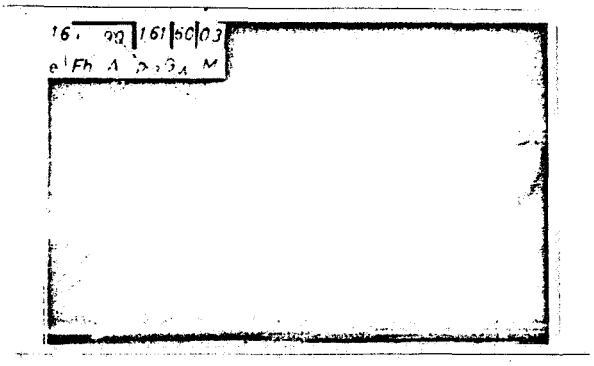

Figure 52

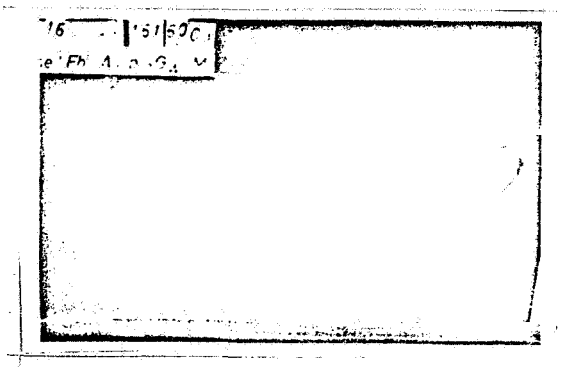

Figure 53

Thereafter the influence of the vaporization becomes evident. The visible jet /59
contour during hot flow remains behind that of cold flow. At the same time the jet becomes more and more transparent until it becomes completely invisible (is completely evaporated) near the end of the test span. The determination of the jet contour during the thermal experiments is more uncertain than during the low-temperature experiments, as can be seen in the illustrations. This is due not only to the more intense blur, because it is not possible to see what has been completely evaporated beyond the visible contour. The values presented below should therefore be regarded merely as a rough approximation or as the lowest limit (maximum reduction of penetration depths). The penetration depths for a number of nozzle headings and distances x (in the direction of the current in the chamber) were plotted y_{hot} against y_{cold} as well as the value $(-\Delta y_{600^o})$ against $(y_c - y_o)$, where y_o is the penetration depth at which the deviation sets in (see Figure 54). After a transition range from y_o to approximately y=100 mm, the thermal contour can be represented as $y_h \approx y_o + 0.5.y_c$ (asymptote). Within the limits of possible measuring accuracy a linear expression can be substituted for the contour variation due to increased temperature between the low-temperature experiment (room temperature) and the thermal headings (t°C). As a result, the law governing the asymptote can be formulated as follows:

$$y_h = \frac{t}{30} + (1 - \frac{t}{1200}).y_c \quad \text{or} \quad y_h = \frac{t}{600}.(20 - 0{,}5.y_c) + y_c \qquad (51a,b)$$

Dimensions: y in mm and t in °C; validity range: $y \geq 100$ mm.

The present law makes possible in good approximation the determination of the hot contours from the cold contours. It is applicable both for parallel stream injection as well as for reverse flow injection.

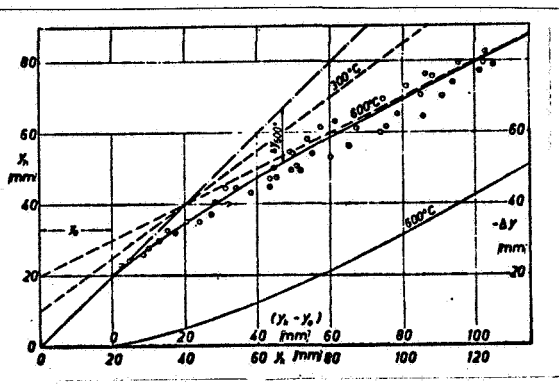

Figure 54. Comparison of low-temperature and high-temperature penetration depths

11. Observation of the Relative Droplet Sizes

11.1. Atomizing Air Ratio and Relative Droplet Size

The question will now be investigated as to what exchange the size of the droplets varies as a result of decreasing atomizing air ratio $\lambda_{AN} = G_A/G_W$. /60

In the process, the prevailing average droplet diameter d is correlated to the value d_1 existing for λ_{AN} and the relative change d/d_1 is examined. This ratio is defined as the average relative droplet size $\bar{d}$: If the ambient pressure and the temperature of the atomizing air remain unchanged, the following relationships may be established:

$$G_A = F \cdot \gamma_A \cdot c_A \qquad \frac{G_A}{G_{A1}} = \frac{c_A}{c_{A1}} \tag{52}$$

$$Ge = \frac{\sigma}{c_A \cdot \eta_A} \qquad \frac{Ge}{Ge_1} = \frac{c_{A1}}{c_A} = \frac{G_{A1}}{G_A} \tag{53}$$

$$Re = \frac{c_A \cdot d}{\nu_A} \qquad \frac{d}{d_1} = \frac{Re \cdot c_{A1}}{Re_1 \cdot c_A} = \frac{Re \cdot G_{A1}}{Re_1 \cdot G_A} \tag{54}$$

If the volume of air is changed for a constant water volume G_W, then

$$\frac{d}{d_1} = \frac{Re}{Re_1} \cdot \frac{G_{A1}/G_W}{G_A/G_W} = \frac{Re}{Re_1} \cdot \frac{\lambda_{AN1}}{\lambda_{AN}} = \frac{Re}{Re_1} \cdot \frac{1}{\lambda_{AN}} \tag{55}$$

The Reynolds numbers can again be determined from the parameter Ge. The value $Ge_1 = \sigma/c_1\eta_1$ is calculated, then the value Re_1 follows from Figure 2. The value Re can also be obtained from Figure 2 with $Ge = Ge_1/\lambda_{AN}$; herewith, the relative droplet size can be determined according to Equation (55). In the following Figure 55, $\bar{d}_m$ is plotted against λ_{AN} with Re_1 and Ge_1 as parameters. In the boundary case of large Reynolds numbers ($Re_1 > 1000$), $\bar{d}_m \approx 1/\lambda_{AN}^2$.

For the experimental investigation of the relative droplet size variation samples were collected from the nozzle jet during atomization of water. Glass plates were employed here; in one case they were coated with a layer of soot and in the other case with a film of oil. The experiments proceeded with a given quantity of liquid with varied ratio of atomizing air. The droplets of one sample differed only little in size from one another (good uniformity). A quantity of average droplets from each sample was taken from the region of greatest abundance, their diameter was measured under the microscope and the average value d calculated therefrom. The introduction of the dimensionless droplet size $\bar{d}_m = d/d_1$ led to the expectation that the errors arising as a result of collecting (bursting or running together of the droplets) would not be manifested as clearly. The values $\bar{d}_m$ determined from the experiments are also reproduced in Figure 55. A dispersion band was found which lies between /61 the boundary curves $\bar{d}_m = 1/\lambda_{AN}$ and $\bar{d}_m = 1/\lambda_{AN}{}^{(1-\lambda_{AN})}$.

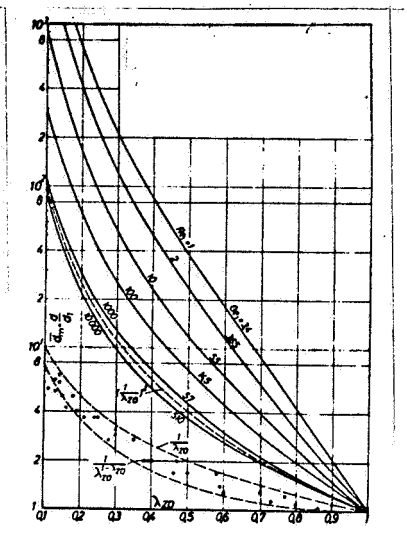

Figure 55. Relative droplet size as a junction of the atomizing air ratio and Re_1 or Ge_1 (calculated and measured curves)

The experimental values are quite low in comparison to the theoretical values especially in the lower λ_{AN} region. Most probably this is due to the uncertain experimental method. The droplets increase in size with decreasing atomizing air ratio. Larger droplets are more prone to bursting upon their collection than are smaller ones at higher λ_{AN} values. It is conjectured, consequently, that the samples collected exhibit a greater number of errors in the lower λ_{AN} range. Experiment and theory, nevertheless, indicated the same tendencies: In the case of a decreasing atomizing air ratio, the quality of the atomization becomes progressively inferior. The smallest, still usable values λ_{AN} are probably found in the vicinity of 0.4 to 0.5.

The nozzle itself as well as the liquid throughput represent determining factors for the absolute droplet size. These influences are not investigated in detail here. The present experiments make it permissible to state that, in the case of larger volumes of liquid, the droplets will increase somewhat with an equal atomizing air ratio, and vice versa. In comparison to solid injections, the quality of the atomization is improved somewhat with small loads.

11.2. Hot Air Atomization and Relative Droplet Size

Even though droplet size was not investigated during the employment of hot air as an atomization medium, this chapter represents an attempt to determine the relative change in the droplet sizes in a theoretical manner. The "cold" nozzle heading (T_o = 300°K) is compared to a number of "hot" nozzle headings, where

at first the air throughput is $G_L = G_{Lo}$ and in both cases the unchanged ambient pressure $p_{st} = p_{sto}$ = atmospheric pressure prevails. The question is posed as to the relationship of the droplet sizes d/d_o as a function of the temperature relationship T/T_o. Equation (14/15) is applied for the droplet sizes:

$$d = \frac{\eta}{\rho \cdot c} \cdot Re = \frac{\eta}{\rho \cdot c} \cdot f(Ge)$$

According to the throughput equation $G = F.\gamma.c$, the following comes true for $G_A = G_{Ao}$: /62

$$\rho \cdot c = \rho_o \cdot c_o \quad \text{or} \quad c/c_o = T/T_o \ (\text{for } p = p_o) \tag{56}$$

The key for the question above consists in the introduction of the Sutherland formula for the variation of the viscosity with temperature:

$$\frac{\eta}{\eta_o} = \left(\frac{T}{T_o}\right)^{\frac{3}{2}} \cdot \frac{(T_o + 120)}{(T + 120)} \tag{57}$$

The relationship of the droplet sizes then becomes:

$$\frac{d}{d_o} = \frac{\eta}{\eta_o} \cdot \frac{Re}{Re_o} = \left(\frac{T}{T_o}\right)^{\frac{3}{2}} \cdot \frac{(T_o + 120)}{(T + 120)} \cdot \frac{f(Ge)}{f(Ge_o)} \tag{58}$$

For the relationship of the parameters Ge can be written with Equation (56) and (57):

$$\frac{Ge}{Ge_o} = \frac{c_o}{c} \cdot \frac{\eta_o}{\eta} = \left(\frac{T_o}{T}\right)^{\frac{5}{2}} \cdot \frac{(T + 120)}{(T_o + 120)} \tag{59}$$

This set of equations can be used in the diagrammatic representation of the relative droplet reduction during hot air atomization (see Figure 56). $Ge_o = \sigma/c_o \eta_o$ is determined for the cold comparison case. Re_o then results from Ge_o according to Figure 2 or Equation (12). Ge is determined by means of Equation (59), where again the Reynolds number is obtained according to Figure 2. Now the relationship d/d_o can be determined according to Equation (58).

The expression used here results in a certain temperature ratio for each Re_o value, where the ratio d/d_o becomes zero. The diagram shows furthermore that for small Re_o values even a slight heating results in a substantial droplet reduction. It was not taken into consideration in the present considerations that an increase in the atomizing air ratio also leads to a heating of the nozzle, so that the fuel flowing through the nozzle is also heated to a certain extent. The resulting changes in the physical fuel properties have not been taken into account. Their effect will probably become evident in an additional reduction of the ratio d/d_o.

The droplet reduction in the hot air atomization can also be explained by means of an energy analysis. Since the head increases with temperature, /63 the temporal energy expenditure also rises with G_A = const. The increased

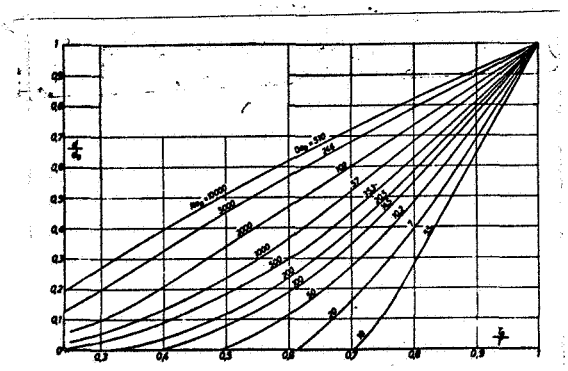

Figure 56. Relative droplet sizes in hot air atomization
(T_o = 300°K)
$G_A = G_{Ao}$
$p = p_o$

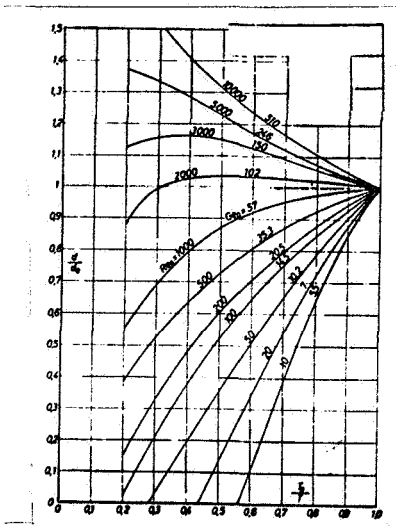

Figure 57. Hot air atomization and relative droplet sizes
$E_A = E_{Ao}$
$p = p_o$
T_o = 300°K

energy expenditure obviously results in an improvement of the atomization. It now becomes a matter of interest what the results would be with equal energy expenditure where the air throughput should be correspondingly reduced upon heating. According to Equation (14/15), the result is again:

$$\frac{d}{d_o} = \frac{Re}{Re_o} \cdot \frac{\eta}{\eta_o} \cdot \frac{\varrho_o c_o}{\varrho c} \qquad (60)$$

According to the throughput equation $G = F.\gamma.c$,

$$\frac{\varrho_o a_o}{\varrho a} = \frac{G_{Ao}}{G_A} \qquad (61)$$

The condition of equal energy expenditure reads:

$$E = G_A H_A = G_{Ao} H_{Ao} \qquad (62)$$

Hence it follows that

$$\frac{G_{Ao}}{G_A} = \frac{H_A}{H_{Ao}} = \frac{a^2}{a_o^2} \qquad (63)$$

Equations (61) and (63) lead to

$$\frac{a_o}{a} = \left(\frac{\varrho}{\varrho_o}\right)^{\frac{1}{3}} \qquad (64)$$

Substitution into Equation (60) results in

$$\frac{d}{d_o} = \frac{Re}{Re_o} \cdot \frac{\eta}{\eta_o} \cdot \left(\frac{\varrho_o}{\varrho}\right)^{\frac{2}{3}} \qquad (65a)$$

From this, together with the gas equation, we obtain at constant ambient pressure $p = p_o$:

$$\frac{d}{d_o} = \frac{Re}{Re_o} \cdot \frac{\eta}{\eta_o} \cdot \left(\frac{T}{T_o}\right)^{\frac{2}{3}} \qquad (65b)$$

By means of Equation (64) and the gas equation the relationship of the parameters Ge takes the form

$$\frac{Ge}{Ge_o} = \frac{\varrho_o \eta_o}{\varrho \eta} = \frac{\eta_o}{\eta} \cdot \left(\frac{T_o}{T}\right)^{\frac{1}{3}} \qquad (66)$$

The last two equations make possible, together with the Sutherland equation, (57) the drawing of a diagram d/d_o against T_o/T at equal energy expenditure $E_A = E_{Ao}$ (see Figure 57). It is surprising that for large Re_o values an increase in droplet size is obtained with rising temperature. The influence of the increasing viscosity predominates here. For Re_o values below approx. 2000 corresponding to $Ge_o < 100$ a reduction of the droplets results, which, as was expected, is not as intense as in the preceding case of equal volumes of air. In order to confirm experimentally the theoretically determined tendencies, the methods of droplet size calculation need to be improved. Such a project, however, is outside of the framework of the present work.

11.3. Ambient Pressure and Relative Droplet Size

All of the jet and droplet investigations have been conducted in atmospheric ambient pressure. Atomizations in an environment of higher pressure could not be conducted in the present experimental unit. It will nevertheless be attempted to estimate the conditions in higher ambient pressures from the results obtained in atmospheric ambient pressure. The atomizing air throughput G_A is left unchanged for the ambient states p_{st1} and p_{st2} compared here. For T = const: $G_A = F.\gamma.c \sim \sqrt{p_{st} \cdot p_{dyn}}$. This, in turn, leads to: /64

$$p_{st1} \cdot p_{dyn1} = p_{st2} \cdot p_{dyn2} \quad \text{or} \quad p_{st2}/p_{st1} = p_{dyn1}/p_{dyn2} \qquad (67)$$

Furthermore, the throughput equation for both cases yields:

$$\gamma_1 \cdot c_1 = \gamma_2 \cdot c_2 \quad \text{or} \quad p_{st2}/p_{st1} = c_1/c_2 \qquad (68)$$

According to Equation (4) and (67)

$$\frac{d_2}{d_1} = \frac{c_{R1} \cdot p_{dyn1}}{c_{R2} \cdot p_{dyn2}} = \frac{c_{R1} \cdot p_{st1}}{c_{R2} \cdot p_{st2}} \qquad (69)$$

is valid. The change in viscosity is obtained from

$$\nu = \frac{\eta}{\varrho} = \frac{\eta . g . R . T}{p_{st}} \sim \frac{1}{p_{st}} \; ; \quad \frac{\nu_2}{\nu_1} = \frac{p_{st1}}{p_{st2}} \qquad (70)$$

The relationship of the Reynolds numbers, by means of Equation (68), (69), and (70) becomes:

$$\frac{Re_2}{Re_1} = \frac{c_2 \cdot d_2 \cdot \nu_1}{c_1 \cdot d_1 \cdot \nu_2} = \frac{C_{R1} \cdot p_{st2}}{C_{R2} \cdot p_{st1}} \qquad (71)$$

Thus, according to Equation (69) and (71):

$$d_2/d_1 = Re_2/Re_1 \qquad (72)$$

The resistance coefficients can be expressed according to Equation (8) in the form:

$$\frac{C_{R1}}{C_{R2}} = \frac{Re_2}{Re_1} \cdot \frac{\sqrt{4 + Re_1}}{\sqrt{4 + Re_2}} \qquad (73)$$

Equation (71) and (73) lead to

$$\frac{p_{st2}}{p_{st1}} = \frac{\sqrt{4 + Re_2}}{\sqrt{4 + Re_1}} \qquad (74a)$$

An increase in the ambient pressure may have as a result that the Reynolds number Re_2, because of the diminishing viscosity ν, falls into the range of Equation (9).

Then

$$\frac{p_{st2}}{p_{st1}} = \frac{0.4 \cdot (200 + Re_2)}{12. \sqrt{4 + Re_1}} = \frac{200 + Re_2}{30. \sqrt{4 + Re_1}} \qquad (74b)$$

The Equations (74a,b) make possible the plotting of the changes Re_2/Re_1 against Re_1 with the pressure ratio p_{st2}/p_{st1} as parameter (see Figure 58). The relationship Re = f(Ge) plotted against Ge is superimposed in this diagram as a broken line; from this, Re_1 can be determined without knowledge of d_1 (see Chapter 3 and Figure 2). For a given atomization case 1, $Ge_1 = \sigma/c_1\eta_1$ is calculated. The dashed line then yields Re_1, and the solid lines in Figure 58 yield the relative change of the Reynolds numbers for specific increases of ambient pressure. /65

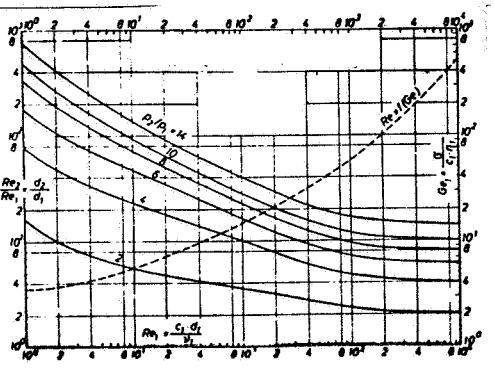

Figure 58. Changes in Reynolds numbers with changes in ambient pressure $G_{A2} = G_{A1}$, $T_2 = T_1$

The result of these considerations may be regarded as very interesting. In accordance with the atomization law Equation (4) the quality of the atomization improves inversely proportional with the ambient pressure. This, however, holds true only with unchanged velocity c_A. On the other hand, a greater γ_A in the case of uniform velocity indicates a higher air throughput. If the same G_A is applied in both cases, then according

to Equation (60) $d_2/d_1 = Re_2/Re_1$. The relationship of the Reynolds numbers, however, increases with increasing pressure (see Figure 58). The quality of the atomization becomes inferior (!) as a result, because the influence of a decreasing velocity is stronger than that of the increased ambient pressure.

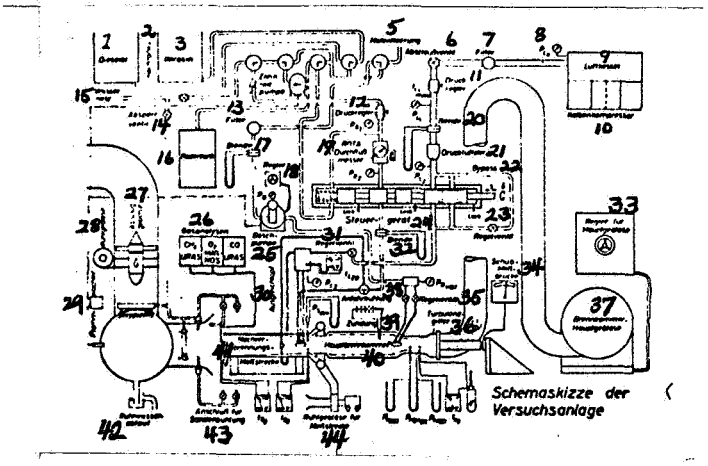

Figure 59. Schematic representation of the test installation

Key:

1. diesel oil
2. overhead tanks
3. kerosene
4. gear pump
5. emergency drain
6. closing valve
7. filter
8. P_{A_C}
9. air boiler
10. piston compressor
11. pressure regulator
12. pressure regulator
13. filter
14. terminal valve
15. water system
16. floor tank
17. diaphragm
18. regulator
19. ROTA throughflow meter
20. diaphragm
21. air-hydraulic lubricator
22. bypass
23. hole
24. control mechanism
25. Bosch pump
26. gas analyses
27. vacuum blower
28. cooling blower
29. flame source
30. balance tank
31. control valve
32. diaphragm
33. regulator for the main blower
34. thrust bridge
35. control valves
36. turbulence grid
37. combustion chamber main blower
38. preliminary cooling
39. ignition
40. main combustion chamber
41. afterburning test section
42. cooling water drain
43. connection for probe cooling
44. cooling blower for test section

PART II

12. General Test Installation and Data Concerning Experimental Combustion Chamber

12.1. General Test Installation

In previous chapters individual parts of the installation have already been described, inasmuch as they related to the experiments carried out there. In the preceding Figure 59 the entire setup is shown schematically, and for reasons of clarity details of lesser importance have been omitted. The photograph, Figure 60, gives an impression of the test installation. The installation mainly consists of the following parts: Combustion chamber-air supply installation, gas exhaust, cooling system, fuel tanks, fuel system for pressure injection, fuel system for air atomization, and air atomization installation.

A large U-shaped bend is connected to the combustion chamber main blower, through which the air at first reaches the combustion chamber entrance test span and subsequently goes into the adjoining combustion chamber, which is /66
suspended so as to swing back and forth. It is supported on a thrust measuring cell. The thrust indication is given through a measuring bridge. The fire tube of the combustion chamber, in order to measure the primary air flow-through, is extended into the intake test section. In the presentation shown in Figure 59 the main combustion chamber is driven with pressure injection, since the amount of atomized air available is not sufficient for main and afterburning.

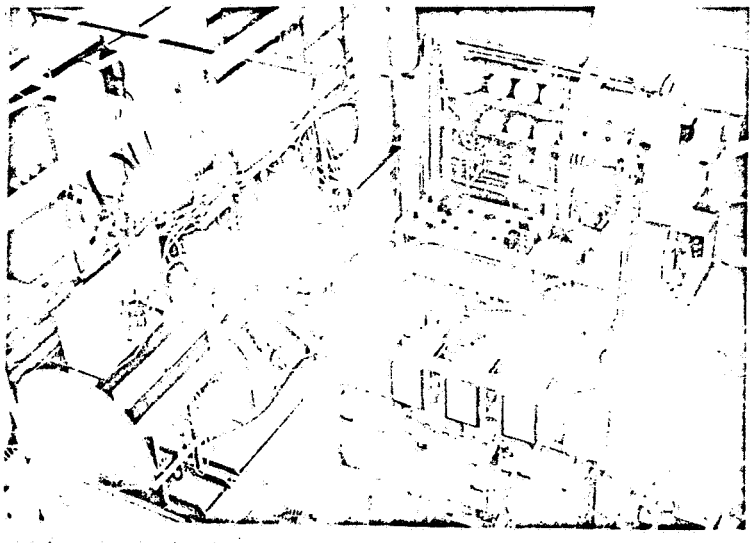

Figure 60

Further details concerning the main combustion chamber are given in Chapter 12.2. Now follows the afterburning measuring section, which has already been described in Chapter 7.2.1. A cooling blower conveys air between the hoods of the test section and produces a cooling veil on the inner walls. At the intake and outlet of the test section, temperature, pressure, and exhaust probes are indicated. The probes had to be equipped with shaft cooling in order to make /67
measurements at the high temperatures (up to about 1800°C) possible. The exhaust gases are received by a funnel, cooled by water injection, and removed by means of a suction blower. The supporting ribs of the suction blower force air from a cooling blower for cooling the motor.

The fuel tank system consists of a floor tank, the overhead tanks, the cog-wheel pump, and a number of three-way cocks. With proper positioning of the cocks, the pump delivers the fuel (kerosene or diesel oil) from the floor tank to the overhead tanks. By changing the position of the cocks, the fuel is delivered from the overhead tanks to the atomization or injection nozzles. Furthermore, provisions are made for the emergency emptying of the tanks, as well as for a connection to the water network for atomization experiments with water.

A fuel filter is installed in the suction pipe of the Bosch pump along with a diaphragm for measuring the flowthrough. The pump first pumps into a chamber in which the injection pressure is measured. From here the fuel is conveyed into the nozzle by way of two regulating valves.

The fuel installation for air atomization, first of all, includes a pressure regulator, after which the tubing branches out. Both branches lead into the control unit (for details see below), where they are sent in opposite directions. The return tubing again leads to the suction side of the cog-wheel pump. In the pipeline to the nozzle, provisions are made for flow-through measurement, in front and behind the control unit (ROTA-flow-through measuring device and diaphragm). Shortly before the nozzle, the fuel pipes are interrupted by a three-way cock, which brings air to the fuel pipes of the atomization nozzle, when we start the main combustion chamber (start-up cooling).

The atomization air is conveyed into the air chamber by a piston compressor. Linked to this are a filter, a pressure regulator, and a measuring diaphragm. Immediately in front of the control unit there is an air pressure oiler, which mixes a very small amount of oil with the air for the lubrication of the control unit. After the oiler the air pipes branch off again into two control unit passages (in order to achieve uniform adjusting paths for the fuel and air control) and one bypass. Over the latter an adjustable quantity of cooling air is conducted, when only the main combustion chamber is being used (control unit closed). After the steering control unit mechanism the three tubes converge again until in front of the nozzle, where they again branch out. One tube leads by way of the single (or several) hollow flameholder of the afterburner test section into the balance tank. The second one also leads into the balance tank by way of the regulating valve for the temperature regulation of the atomization air (cold air admixture). The third branch pipe constitutes the above-mentioned /68
start-up cooling pipe of the fuel pipe to the nozzle. In the balance tank, temperature and pressure measuring stations are installed. From here, two air pipes lead into the (triple-flow) nozzle of the afterburner measuring section.

The control valve pictured here is the end product of extensive experiments (see research reports Tr. 13/7, 13/11, 13/15). At first, directly working systems were examined. Here one of the two nozzle media operated the control valve through changes in pressure attained by way of a throttle valve. In this way, the cross section of the current of the other medium was changed, so that its flowthrough, at a constant entrance pressure, changed in the same direction as the flowthrough of the control medium because of its change in pressure. Because of the low pressure level of the two media, the influence of friction was quite noticeable in the adjusting joints. In order to eliminate the problems caused by friction a change to indirect control was made. The test apparatus is provided with direct, single-lever manual operation. In the practical application, a compressed-oil-controlled cylinder or an electromagnetic tension rod can be introduced. Whereas the fuel passages are controlled directly by the piston edges, the air passages through the control valve are formed as diagonal holes in the control piston. If we have a certain fuel flowrate, that is, if we have a certain axial piston position, this makes it possible to vary the air flowthrough within wide limits and consequently the atomizing air ratio by turning of the piston.

12.2. Test Chamber

The first systematic thermal tests were conducted with an antiquated JUMO 004 combustion chamber. The results attained in this case however were not satisfactory. By means of construction changes on the chamber, improvements could be made, but the present state of a high-performance combustion chamber could not nearly be reached. In order to create suitable conditions for the hot tests which were to be performed, a new chamber was planned. In designing this test chamber, we come close to the upper limits of empirical design data in order to test the atomization system under the most difficult circumstances.

A summary of the most important points to be taken into account in constructing the chamber was given in research report Tr. 13/18. This mainly concerned the observation of ignition lags and the relationships and effects of /69
their parameters (air, droplet, or steam temperature, size of droplets, air pressure, etc.). The strongest parameters are temperature and pressure of the ambient air in the chamber. The larger these two values, the shorter the ignition delays. In order to keep the first phase of the ignition delay time (the heating and evaporation period) as short as possible, a sharp rise in temperature must be provided. This is accomplished by a partial gas reflux in localized vorteces (macroturbulence). The faster heating of the smaller droplets is counteracted by a resultant temperature reaction; in case of a large air surplus, we only get a minor temperature drop while in the rich range we get a strong cooling effect when we have fine-grade atomization. A local reduction in oxygen is connected with the evaporation because the steam concentration rises near the drops. It is necessary to compensate for this local impoverishment in oxygen and to homogenize the mixture. This is done through the creation of a strong microturbulence. This means vorteces in a very small space, which are not localized but swim with the current.

In extensive fire tube tests certain guiding principles for the air circulation in the chamber have emerged. These are in agreement with the briefly mentioned general observations above. Figure 61 shows a scaled schematic representation of the test chamber which was determined to be the best. Of the calculated primary air (see below) only about half flows frontally into the fire tube; the rest flows through the holes in the wall in the forward part of the flame tube (section I; zone of separation and primary reactions). It was most advantageous for the fuel system examined to convey the remaining primary air, approximately at the turning point, to the return current zone, which was induced by the wide-angle hollow jet of the nozzle or by the flameholder. Because of this the return current became quite hot and rich in oxygen. By means of the mounting of sheet metal traps on the fire tube, the total pressure of the outer air current could be used for the penetration. The number of supply openings on the circumference for the remaining primary air is most efficiently made an odd number in order to avoid transverse vibrations.

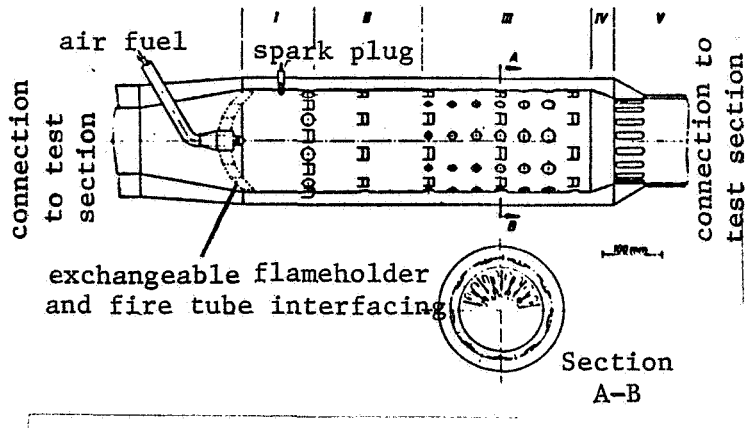

Figure 61. Experimental Combustion Chamber
(schematic, scaled)

The actual combustion zone is connected to section I of the fire tube. Because of the ignition delays (maintenance of high temperature), no further air is conducted into the fire tube in the first part of the combustion zone (section II) with the exception of a thin cooling veil on the inner wall. In the following section III the gradual addition of the secondary air begins. For this addition of air, a number (also odd) of rows of holes along the fire tube jacket is suitable, where the holes increase in size toward the end of the /70
fire tube. The air which comes through the rows of holes causes a radial current toward the outside, in the area between the rows (see cross section, Figure 61). In this way a very good distribution of oxygen and temperature is achieved over the cross section. Between the rows of holes, cool folds are to be installed, because the hot gases streaming towards the outside could otherwise easily destroy the fire tube.

After section III, where about half of the secondary air is added, a small acceleration occurs in section IV. In this way, the speed profile is equalized, because the border zones are accelerated more than the central ones. Furthermore, the acceleration results in a decrease of the static pressure, which makes it easier for the rest of the secondary air to enter at the beginning of section V (mixing zone). Through this locally intensive admixture of air, the

temperature is reduced considerably, so that practically no further combustion reactions result. Along the mixing zone, in the practical application, current and temperature profile are adapted to the turbine blades. The test chamber ends with a test span where a cooling veil serves to bring about low wall temperatures.

The main blower available for the test stand delivers a 2 kg/sec flow-through at 1500 mm WC total pressure increase. The combustion chamber, therefore, reveals experimental conditions that are the same as those at flying altitudes more than 10 km. Since the combustion deteriorates as the flying altitude increases, this fact must be taken into account when the subsequently measured η_C performances are considered.

The size of the combustion chamber (the volume) is determined from the heat load. The latter is defined as the heat introduced per time unit, in relation to the volume of the fire tube and the absolute static entrance pressure:

$$B = \frac{Q_{perm}}{V_{FlT} \cdot P_{ost}} = \frac{Q_{perm}}{(V_{CoC} + V_{MC}) \cdot P_{ost}} \quad \frac{kcal}{h.m^3.atm\ abs} \tag{75}$$

Subscripts: FlT = flame tube, CoC = combustion chamber, MC = mixing chamber. /71
A further important design parameter consists of the chamber air ratio $\mu = g_{Apr}/g_{Atot}$. This value, first of all, is a function of the rated temperature T_R. For the theoretical temperature increase ΔT_{th}, in the case of kerosene, we have a diagram in which ΔT_{th} is plotted, taking into account the dissociation against the specific fuel consumption $b_1 = g_F/g_A$ with the combustion chamber entrance temperature T_{ot} as a parameter (see Figure 62). Superimposed is the relationship $\lambda_{tot} = \lambda_{pr}/\mu$ (straight line group). With a desired increase in temperature ΔT_{act} and with an assumed η_C the necessary air ratio can be determined, according to the arrows drawn. The reproduction of the whole design computation has been omitted here. Only the most important chamber data are shown below; in the parentheses usual construction ranges are given.

Desired temperature increase: $\Delta T_{act} = 850°$

Rated temperature: $t_{5t} = 880°C$; $T_{5t} = T_R \approx 1150°K$

$\Delta T_{th} = \Delta T_{act}/\eta_C = 880°$; $\mu = 0.33$; $\lambda_{tot} = 3$

Fuel quantity: gF = 165 kg/hr; heat supply: $Q_{perm} = 1.7 \cdot 10^6$ kcal/hr

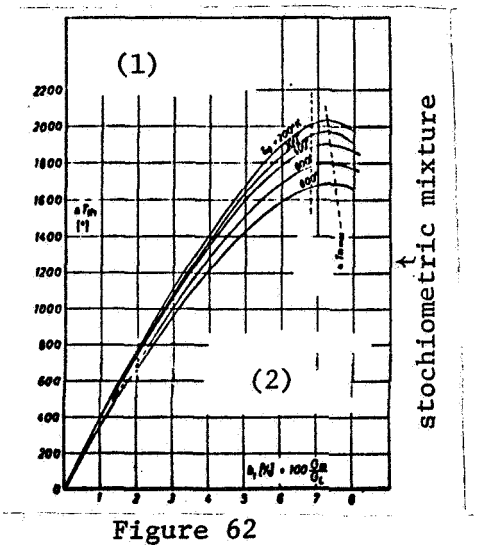

Figure 62

1. Theoretical increase in temperature during combustion of kerosene (dissociation accounted for)
2. In the understochiometric range
$T_{th} = T_{th300°K} - 8b_1 \cdot (T_{ot} = 300)$
is valid for
$200°K < T_{og} < 800°K$

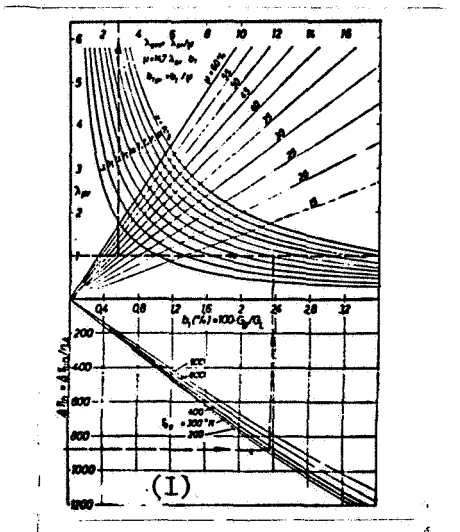

Figure 63

1. Necessary air ratio $\mu = G_{Apr}/G_{Atot}$ for rated temperature

Flame tube load: $L = 75.10^6$ kcal/hr m^3 atm abs; (for highly loaded propulsion units L usually is within the range 40 to 80.10^6 kcal/hr m^3 atm abs). /72

Flame tube volume: $V_{FlT} = V_{CoC} + V_{MC} = 0.02$ m^3

Time in combustion chamber: $t_L = 2.5 \cdot 10^{-3}$ sec; (usually 2 to $8 \cdot 10^{-3}$ sec)

Volume of combustion chamber: $V_{CoC} = 0.015$ m^3; mixing chamber volume: $V_{MC} = 0.005$ m^3

Length of combustion chamber $\ell_{CoC} = 0.65$ m

Mach number at combustion chamber, intake: $M_o = 0.17$; (usually 0.15 to 0.2)

Mach number after flameholder; cold: $M_{IIc} = 0.065$; (0.03 to 0.07)

Mach number after flameholder; hot: $M_{IIh} = 0.18$; (0.1 to 0.2)

Mach number at end of combustion chamber $M_{III} = 0.32$; (0.2 to 0.3)

Velocity at end of combustion chamber: $c_{III} = 255$ m/sec

Maximum Mach number at end of mixing chamber: $M_V = 0.55$; (0.25 to 0.35)

Maximum speed at end of mixing chamber: $c_V = 370$ m/sec